

<https://doi.org/10.1038/s42003-025-08576-w>

HEP14 treatment improves ovarian function in aged mice through mitophagy enhancement and oxidative stress reduction

Check for updates

Liming Gui ^{1,2,3}✉, Jiajia Sun ^{1,2}, Qin Zhong ^{3,7}, Kan Liu ^{1,2}, Qili Sun ⁴, Yingtong Di ⁵, Helen Picton ⁶, Bin Tang ⁴✉, Xiaojiang Hao ⁵✉ & Changzhong Li ^{1,2}✉

Ovarian aging profoundly impacts reproductive health and accelerates the overall aging process, yet the development of effective therapeutic strategies remains a formidable challenge. In this study, we report the rejuvenating effects of HEP14, a natural activator of protein kinase C (PKC) pathway, on aged ovarian function by inducing mitophagy and effectively clearing reactive oxygen species. To ensure controlled and sustained delivery of HEP14 *in vivo*, we develop HEP14-loaded PLGA microspheres. Transcriptomic analysis reveals a significant overlap between the transcriptional profiles of HEP14-treated aged ovaries and those of adult ovaries, suggesting molecular rejuvenation process closely associated to HEP14-induced mitophagy. Histopathological evaluations further substantiate these findings, showing that HEP14 enhances mitophagy, exhibits antioxidative properties and promotes follicular regeneration. Consequently, ovarian endocrine function in aged mice is substantially restored. Using transmission electron microscopy, confocal microscopy, and western blot analysis alongside pharmacological inhibitors and PKC-specific siRNA, *in vitro* studies further demonstrate the restorative effect of HEP14 on mitophagy, leading to improved mitochondrial function and subsequent alleviation of oxidative stress in senescent ovarian granulosa cells. This effect is mediated through the activation of the PKC-ERK1/2 pathway, which plays a pivotal role in the action mechanism in HEP14. These discoveries offer new therapeutic hope for ovarian aging.

Aging-related senescence refers to the gradual degeneration of organ and tissue functions with age. Ovarian aging becomes apparent earlier in a woman's lifespan than aging in other systems, marked by a decline in both the quantity and quality of ovarian follicles. This decrease ultimately leads to reduced estrogen production, heralding the onset of menopause and a myriad of associated comorbidities that seriously endanger women's physical and mental health. International research on treatment strategies for ovarian decline has been ongoing and intensifying^{1–4}.

Throughout the aging process, mitochondria undergo persistent stress and depletion, leading to an accumulation of reactive oxygen species (ROS) and subsequent mitochondrial impairment⁵. This impairment is now widely recognized as a pivotal contributor to the aging of the body, including the ovaries. Mitophagy, known as mitochondrial autophagy, is a specialized form of autophagy that selectively targets and degrades damaged mitochondria. This process is crucial for maintaining mitochondrial integrity and preventing ROS

¹Department of Obstetrics and Gynecology, Peking University Shenzhen Hospital, Shenzhen, China. ²Institute of Obstetrics and Gynecology, Shenzhen Peking University-Hong Kong University of Science and Technology (PKU-HKUST) Medical Center, Shenzhen, China. ³Centre for Tissue Engineering and Stem Cell Research, Guizhou Medical University, Guiyang, China. ⁴Department of Biomedical Engineering, Southern University of Science and Technology, Shenzhen, China. ⁵State Key Laboratory of Phytochemistry and Plant Resource in West China, Kunming Institute of Botany, Chinese Academy of Sciences, Kunming, China. ⁶Reproduction and Early Development Research Group, Discovery and Translational Science Department, Leeds Institute of Cardiovascular and Metabolic Medicine, School of Medicine, University of Leeds, Leeds, UK. ⁷Present address: Clinical Medical Research Center, Affiliated Hospital of Guizhou Medical University, Guiyang City, Guizhou Province, China. ✉e-mail: dawnkwei@163.com; tangb@sustech.edu.cn; haoxj@mail.kib.ac.cn; 15168888909@163.com

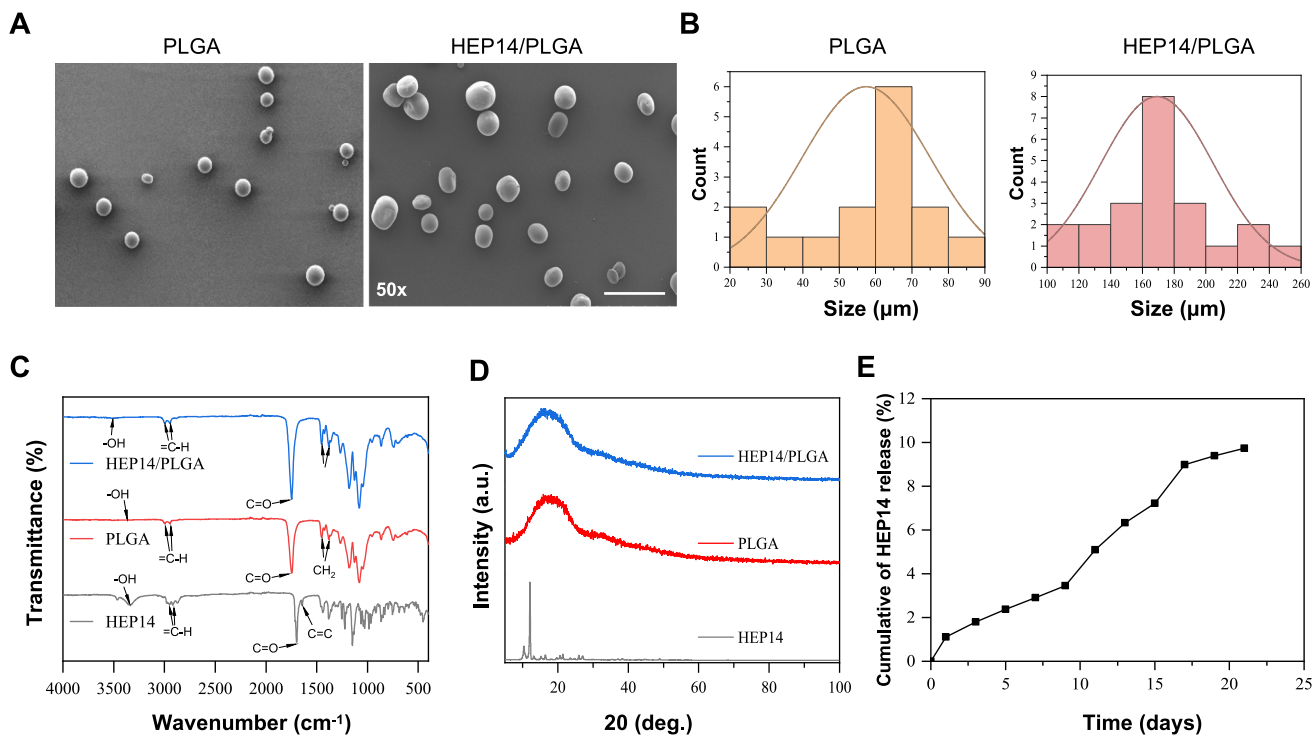


Fig. 1 | Characterization of HEP14-loaded PLGA microspheres. **A** Representative SEM images of PLGA and HEP14/PLGA microspheres. **B** Size distribution curves for PLGA and HEP14/PLGA microspheres. **C** FTIR spectra of HEP14/PLGA-,

PLGA microspheres and HEP14. **D** XRD patterns of HEP14/PLGA-, PLGA microspheres and HEP14. **E** Release curve of HEP14/PLGA microspheres *in vitro*. Scale Bar, 500 μ m.

buildup, thereby emerging as a key factor in delaying the aging processes^{6,7}.

Granulosa cells (GCs) are the primary functional cells of the ovaries and have a direct impact on follicular atresia and the overall functional activities of the ovaries⁸. These activities encompass the initial development and maturation of follicles as well as the secretion of steroid/endocrine hormones. The integral functionality of mitochondria within GCs holds utmost significance in maintaining ovarian function. As GCs age, mitochondrial dysfunction may ensue, triggering follicular atresia^{8,9} and aberrant estrogen production. This, in turn can accelerate ovarian aging and give rise to a range of estrogen-dependent disorders¹⁰. Recent research advancements indicated that pharmaceutically enhancing mitophagy can enhance mitochondrial function¹¹. This underlines the critical need to identify signaling pathways or molecules capable of regulating cellular mitophagy, as a means to counteract ovarian aging.

HEP14, a natural compound, has recently identified as a novel activator of the protein kinase C (PKC) pathway¹². PKC is a family of serine/threonine kinases that act upstream of the mitogen-activated protein kinases (MAPKs), specifically MAPK1/3, also known as extracellular signal-regulated kinases 1 and 2 (ERK1/2). These kinases are linked to the induction of autophagy^{13,14}. However, the mechanism that PKC modulates mitophagy remains unknown. Our drug screening investigations revealed that HEP14 can revitalize hydrogen peroxide (H_2O_2)-induced senescent KGN cells. KGN cells, widely used to model primary ovarian granulosa cells¹⁵, offer a relevant system to study HEP14's effects on granulosa cell function. Interestingly, this rejuvenating effect of HEP14 was abrogated by the administration of Mdivi-1, a mitophagy inhibitor^{16–20}. Chloroquine (CQ), a lysosome inhibitor and PKC-specific siRNA¹². This suggests that the HEP14-activated PKC signaling pathway may play a role in the regulation of mitophagy and mitochondrial function in senescent ovarian GCs, therefore potentially contributing to the rejuvenation of ovarian function.

To overcome the poor aqueous solubility of HEP14 and achieve a sustained release of HEP14 in *in vivo* circulation, we used Poly(lactic-co-glycolic acid) (PLGA) as a drug carrier to fabricate HEP14-loaded PLGA

microspheres (referred as to HEP14/PLGA microspheres). In this study, treatment utilizing HEP14/PLGA microspheres *in vivo* substantially restored the transcriptomic profile of aged ovaries in the model mice used, closely resembling that of adult ovaries. Further integration of *in vitro* and *in vivo* data revealed that HEP14 promoted ovarian regeneration and rejuvenated ovarian endocrine function through activation of PKC-ERK1/2-mitophagy signal cascades. As such, HEP14 emerges as a promising prospect for the advancement of pharmacotherapeutic approaches aimed at rejuvenating aged ovaries and addressing menopausal disorders.

Results

HEP14-loaded PLGA microspheres displayed a sustained release of HEP14

To investigate the anti-aging properties and mechanisms of HEP14, we first prepared HEP14/PLGA microspheres for an *in vivo* study in aged mice. The microspheres were fabricated via the single emulsion solvent evaporation technique. Scanning electron microscope (SEM) analysis confirmed the uniform size distribution and spherical shape of both PLGA and HEP14/PLGA microspheres with smooth surfaces, crucial for consistent drug release and bioavailability (Fig. 1A). The size of HEP14/PLGA microspheres ($0.1688 \text{ mm} \pm 0.0685$) was significantly larger than that of pure PLGA microspheres ($0.052 \text{ mm} \pm 0.028$), attributed to the effective drug loading (Fig. 1B). Fourier transform infrared spectroscopy (FTIR) were conducted to verify the encapsulation of HEP14 within the PLGA matrix. The absence of specific HEP14 vibration peaks in the HEP14/PLGA microspheres suggested successful encapsulation (Fig. 1C). X-ray diffraction analysis (XRD) further supported this result that the crystalline peak of HEP14 disappeared upon encapsulation, leading to enhanced gradual release (Fig. 1D). A standard curve at 201 nm ($y = 0.0785c + 0.1555$, $R^2 = 0.9966$, $n = 6$) was established to quantify the HEP14 loading and encapsulation rates, which was 3.10% and 18.04%, respectively, confirming effective drug incorporation into the PLGA matrix. *In vitro* release kinetics by ultraviolet spectrophotometry showed an initial burst release followed by a sustained release over 9 days, with a cumulative release of ~9.73% of HEP14 (Fig. 1E),

indicative of a controlled release mechanism that should enhance the therapeutic's anti-aging effects *in vivo*.

HEP14 changed ovarian transcriptome profile in aged mice

To delve into the molecular mechanisms underlying HEP14-driven restoration of ovarian function in aged mice, we conducted a comparative transcriptomic analysis (accession code: GSE273724) on ovaries from five groups of mice: young (7–8 weeks; young mice), adult (27–28 weeks) treated with either vehicle (adult mice) or HEP14 (adult+HEP14 mice), aged mice (73–74 weeks) treated with either vehicle (aged mice) or HEP14 (aged+HEP14 mice). Principal component analysis (PCA) and column-clustered heatmaps revealed that HEP14-treated aged ovaries exhibited a transcriptional profile closely resembling those of adult ovaries and HEP14-treated adult ovaries, and distinct from both young and untreated aged ovaries (Fig. 2A, B). Additionally, a transcriptional profile of adult ovaries clustered with that of HEP14-treated adult ovaries (Fig. 2B). Pearson correlation coefficient (PCC) analysis confirmed the high reproducibility of the data with minimal biological variability within groups ($R^2 = 0.799$ –0.992; Fig. S1A). Volcano plots highlighted significant differential expression genes (DEGs) in HEP14-treated versus untreated aged ovaries, with 5422 upregulated and 4615 downregulated DEGs (Fig. 2C). Compared to adult ovaries, 1608 DEGs were upregulated and 953 DEGs downregulated in the HEP14-treated aged ovaries (Fig. 2D), while 734 DEGs were upregulated and 886 DEGs were downregulated in the HEP14-treated adult group (Fig. 2E). In contrast, 5563 DEGs were upregulated and 5948 DEGs downregulated in the untreated aged ovaries compared to adult ovaries (Fig. S1B). These findings suggest a substantial transcriptional restoration in the HEP14-treated aged ovaries, which was not observed in the HEP14-treated adult ovaries. Gene Ontology (GO) and Kyoto Encyclopedia of Genes and Genomes (KEGG) analyses provided insights into the underlying biological processes, with enrichment in terms like autophagy, response to oxidative stress (Fig. 2F) and in pathways such as autophagy, protein processing in endoplasmic reticulum, and endocytosis (Fig. 2G). Gene set enrichment analysis (GSEA) further supported HEP14's role in modulating specific signaling pathways related to mitophagy, oxidative stress response, steroid hormone biosynthesis and PKC binding in the HEP14-treated aged ovaries (Fig. 2H–K). Altogether, our findings suggest that HEP14 reset the transcriptional pattern of the aged ovary to what is closely similar to that of the adult ovary.

HEP14 induced mitophagy to counteract oxidative stress in aged ovaries

Furthermore, we reconstructed a sub-heatmap that included 54 recovered DEGs enriched in autophagy and mitophagy pathways within HEP14-treated aged ovaries (Fig. 3A). Mitophagy is characterized by the formation of mitophagosomes that fuse with lysosomes to form mitolysosomes. We further examined mitophagy markers Voltage-dependent anion channel 1 (Vdac1)^{21–23}, PTEN induced putative kinase 1 (Pink1)²⁴, autophagy markers microtubule-associated protein light chain 3 (Map1lc3)²⁵, autophagy receptor Sequestosome 1 (Sqstm1)²², and lysosome marker Lysosomal associated membrane protein 2 (Lamp2)^{26,27}. Consistent with the RNA-seq data (Fig. 3A, B), immunofluorescence (IF) double or triple staining demonstrated that Map1lc3, Sqstm1, Vdac1 and Lamp2 signals all significantly increased in the HEP14-treated aged ovaries compared to those in the aged ovaries. Map1lc3 and Sqstm1 signals overlapped (Fig. 3C), and Vdac1 signals colocalized with Map1lc3 and Lamp2 signals (Fig. 3D; Fig. S2A). Immunohistochemical (IHC) staining further confirmed the marked increases in the expression of Pink1, Map1lc3 and Sqstm1 in HEP14-treated aged ovaries (Fig. S2B–D). These findings indicate that HEP14 treatment may enhance mitophagy and promote the formation of mitolysosomes. Ovarian cell senescence is accompanied by mitochondrial dysfunction and excessive production of ROS. Our RNA-seq analysis revealed that HEP14 restored mRNA levels of 43 DEGs associated with the response to oxidative stress in the HEP14-treated aged ovaries, to levels closely similar to those in adult ovaries (Fig. 3E). IHC staining of ovarian sections verified our RNA-

seq findings (Fig. 3F), showing significantly enhanced protein expression of the crucial and representative antioxidant genes Catalase (CAT), Thioredoxin-like protein-1 (Txnl1) and Heme Oxygenase-1 (Hmox1) in the HEP14-treated aged ovaries, respectively (Fig. 3G–I). These results imply that HEP14 treatment reinforces anti-oxidative mechanisms in aged ovaries. Together, our findings suggest that HEP14 potentiates mitophagy and alleviates oxidative stress in ovarian cells from aged mice.

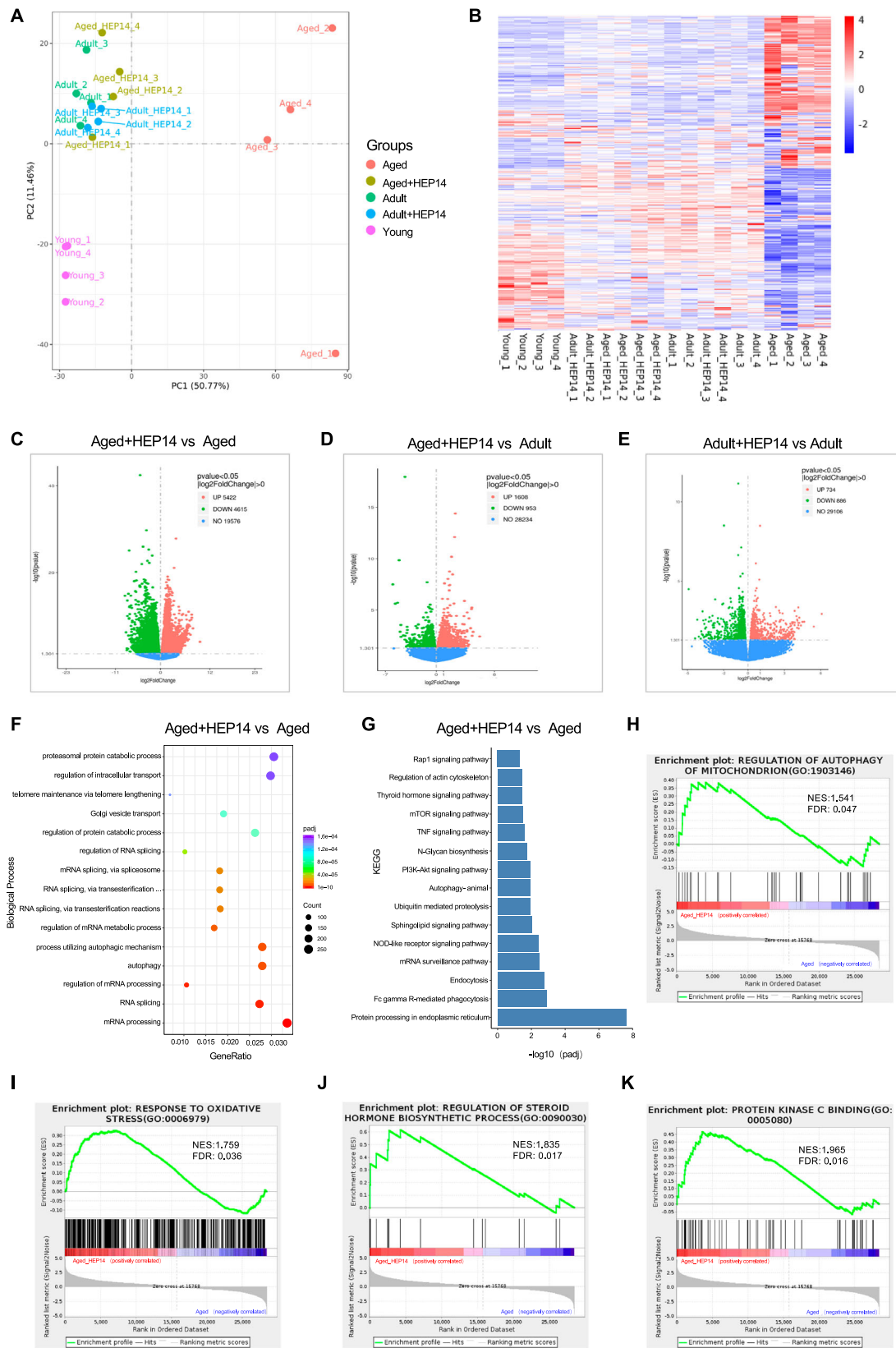
HEP14 enhanced mitophagy and facilitated mitochondrial function by maintaining mitophagic flux in senescent KGN cells

GCs, essential for ovarian function, respond to gonadotropins to produce steroids and promote follicle development. This is a mitochondrial-dependent process^{28,29}. To investigate the role of HEP14 in mitophagy and its potential to rejuvenate senescent GCs, 75 μ M H₂O₂, following concentration optimization, was used to induce senescence of KGN cells (Fig. S3A–C). The senescence phenotype of KGN cells was confirmed by several key indicators: increased signals in SA- β -Gal and γ H2AX staining, the absence of Ki-67 expression by IF staining (Fig. 4A–C), and a marked increase of vacuoles within the mitochondria accompanied by a reduction in the number of mitochondria, as observed (Fig. 4E, yellow arrows) compared to those in control cells (Fig. 4D, red arrows) by transmission electron microscope (TEM). These changes are indicative of mitochondrial senescence. HEP14 treatment significantly restored senescent KGN cell viability compared to control cells, as evidenced by CCK8 and PicoGreen (a DNA-binding dye) staining assays (Fig. 4F; Fig. S3D, E). This dye fluoresces when bound to DNA, which enables quantification of the total DNA content and assessment of cell number. However, this effect was largely abolished by the presence of mitophagy inhibitor Mdivi-1 or CQ (Fig. 4F), highlighting the importance of mitophagy pathway in mediating rejuvenating effects of HEP14.

Moreover, IF staining revealed that HEP14 augmented signals of MAP1LC3 and SQSTM1 in senescent KGN cells (Fig. S3F, G). Fluorescence staining using LysoTracker and MitoTracker (Fig. 4G and Fig. S3H), as well as LysoTracker and VDAC1 (Fig. 4H; Fig. S3I), demonstrated an increased colocalization, indicating the fusion of mitophagosomes with lysosomes and the effective transfer of mitochondrial material to the lysosome. TEM analysis provided direct evidence that HEP14 boosted quantity of mitochondria and formation of mitolysosomes, identified by the presence of the double membrane and remnant of the cristae structure³⁰ in senescent KGN cells (Fig. 4J, blue arrows) compared to untreated senescent KGN cells (Fig. 4I, yellow arrows), which contained a large number of vacuolized mitochondria. These effects were diminished by Mdivi-1 or CQ. Co-treatment with Mdivi-1 led to increased vacuolized mitochondria (Fig. 4K, yellow arrows) and residual mitochondrial myeloid bodies (Fig. 4K, purple arrows), indicative of mitochondria with impaired function, while co-administration with CQ resulted in an increase in swell mitochondria (Fig. 4L, yellow arrows) and the formation of larger mitolysosomes containing undegraded mitochondria (Fig. 4L, blue arrows), indicating an impeded mitophagy flux. These findings supported that HEP14 promoted formation of mitolysosomes and mitophagic flux. Western blot analysis revealed an elevation in the expression levels of MAP1LC3-II, SQSTM1, VDAC1, and PINK1 following HEP14 treatment (Fig. 4M). However, co-treatment with Mdivi-1 compromised these effects, whereas co-treatment with CQ resulted in increased accumulation of MAP1LC3, SQSTM1 (Fig. 4M). This further substantiated that HEP14 facilitated the clearance of damaged mitochondria and sustained the mitophagic flux. Altogether, our findings demonstrate that HEP14 treatment effectively enhanced mitophagy in senescent granulosa cells by promoting the formation of mitolysosomes and maintaining the integrity of the mitophagic flux, thereby potentially improving mitochondrial function.

HEP14-enhanced mitophagy protected senescent KGN cells against oxidative stress by improving mitochondrial function

There is a close relationship between mitophagy, mitochondrial function, and the production of intracellular ROS. To investigate the impact of



HEP14-enhanced mitophagy on mitochondrial function, we measured the mitochondrial membrane potential ($\Delta\Psi_m$) and quantified ROS production. The JC-1 staining showed a significant increase in the ratio of J-aggregates to JC-1 monomers in HEP14-treated senescent KGN cells compared to untreated cells, indicating an increased $\Delta\Psi_m$ level associated with enhanced mitochondrial function (Fig. 5A and Fig. S4A). To further evaluate

mitochondrial function, we conducted co-staining using MitoSox and MitoTracker, as well as staining with H2DCFDA. MitoSox is a highly selective fluorescent probe that specifically targets mitochondria and is oxidized by superoxide, producing intense red fluorescence. The fluorescence intensity is directly proportional to the level of ROS within the mitochondria³¹, while H2DCFDA, also known as

Fig. 2 | Transcriptome profiling of ovaries in HEP14-treated aged mice.

A Principal-component analysis (PCA) was performed on samples obtained from ovaries of young mice, adult mice and adult + HEP14 mice, as well as aged mice and aged + HEP14 mice. **B** Heatmap data shows differentially expressed genes (DEGs) among five groups. **C** Volcano plot exhibits upregulated and down-regulated DEGs between HEP14-treated aged ovaries and aged ovaries. **D** Volcano plot displays upregulated and down-regulated DEGs between HEP14-treated aged ovaries and adult ovaries. **E** Volcano plot illustrates upregulated and down-regulated DEGs

between HEP14-treated adult ovaries and adult ovaries. DEGs were identified according to the criteria: $|\log_2 \text{FC}| = 0$ and $\text{adj } p < 0.05$. Upregulated genes are indicated in red, while downregulated genes are indicated in green. **F** Gene Ontology (GO) enrichment analyses of DEGs for the biological processes and **G** Kyoto Encyclopedia of Genes and Genomes (KEGG) pathway analyses of DEGs in HEP14-treated ovaries compared to aged counterparts by clusterprofiler 3.8.1. **H–K** Gene Set Enrichment Analysis (GSEA) evaluates the influence of HEP14 on GO terms by gsea v3.0. $n = 4$ biological replicates.

2',7'-dichlorodihydrofluorescein diacetate, is a redox-sensitive fluorescent probe used to measure intracellular ROS levels³². We observed a significant reduction in ROS production in HEP14-treated senescent KGN cells compared to control senescent KGN cells (Fig. 5B, C; Fig. S4B). This suppressive effect on ROS generation was largely reversed by the addition of Mdivi-1 and CQ (Fig. 5B, C), demonstrating that HEP14's effect to reduce ROS production is dependent on the mitophagy pathway. Furthermore, western blotting revealed that HEP14 treatment led to an upregulation of critical antioxidant genes CAT, TXNL1 and HMOX1 (Fig. 5D). This upregulation was significantly abrogated when cells were co-treated with the mitophagy inhibitor Mdivi-1 and the lysosome inhibitor CQ (Fig. 5D), suggesting that HEP14 upregulated antioxidant gene expression through the mitophagy pathway. These data together suggest that HEP14 strengthened mitochondrial function and combated oxidative stress through the activation of mitophagy.

HEP14-activated PKC-ERK1/2 pathway is required for mitophagy enhancement and ROS clearance in senescent KGN cells

The RNA-seq analysis suggested that DEGs related to molecular function were enriched in PKC binding within the ovaries of aged mice treated with HEP14 (Fig. 2K). PKC functions upstream of ERK1/2, and activated ERK1/2 strengthens autophagic flux^{13,14}. RNA-sequencing data revealed a marked upregulation of ERK1/2 in the HEP14-treated aged ovaries versus controls (Fig. 6A). IHC staining of ovarian sections demonstrated a significant increase in the expression of phosphorylated PKC (pPKC), ERK1/2, and phosphorylated ERK1/2 (pERK1/2), implicating the PKC-ERK1/2 signaling pathway in HEP14-mediated mitophagy (Fig. 6B–D). To further investigate the mechanistic underpinnings, we employed pharmacological inhibitors that specifically target PKC (Go6850) and ERK1/2 (U0126) in senescent KGN cell culture. MitoTracker green and Lysotracker red co-staining (Fig. 6E) showed an increase in colocalized signals in senescent KGN cells treated with HEP14, indicating enhanced mitophagy. Furthermore, co-staining experiments employing MitoSox and MitoTracker, along with staining using H2DCFDA, demonstrated a reduction in ROS production following HEP14 treatment (Fig. 6F, G). However, these effects were effectively abolished when cells were simultaneously co-treated with either Go6850 or U0126 (Fig. 6F, G), suggesting the involvement of PKC and ERK1/2 signaling pathways in the observed mitophagic response and ROS reduction. Further TEM analysis supported these findings, showing that HEP14 treatment effectively facilitated clearance of vacuolized mitochondria, as observed in control cells (Fig. 6H, yellow arrows), and replaced these damaged mitochondria with substantial number of mitochondria exhibiting regular shape and well-organized cristae structures (Fig. 6I, red arrows), and induced formation of mitolysosomes (Fig. 6I, blue arrows). However, co-treatment with either Go6850 (Fig. 6J, yellow arrows) or U0126 (Fig. 6K, yellow arrows) abrogated these effects of HEP14 on senescent KGN cells, resulting in an increased number of vacuolized mitochondria.

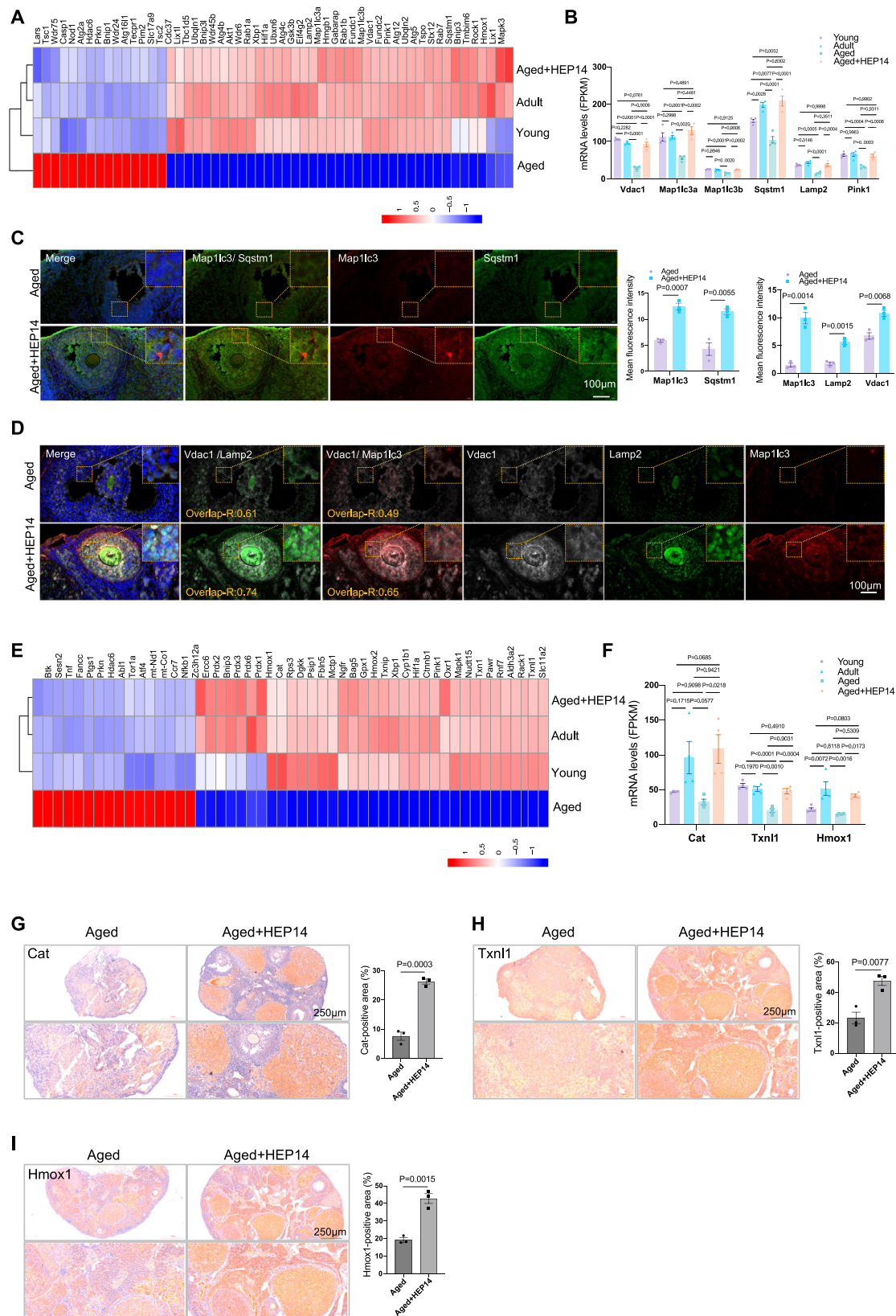
Western blot analysis presented convincing evidence that HEP14 stimulated the phosphorylation of PKC and ERK1/2, leading to elevated levels of autophagosome markers MAP1LC3 and SQSTM1, mitophagy markers VDAC1 and PINK1 (Fig. 6L), as well as upregulation of antioxidant genes CAT and TXNL1 (Fig. 6M). However, co-treatment with U0126 effectively abrogated these effects, while co-administration with Go6850 inhibited HEP14-induced phosphorylation level of PKC and ERK1/2. The inhibition not only attenuated the HEP14-induced elevation of VADC1, PINK1, CAT and TXNL1 expression but also resulted in the accumulation of MAP1LC3

and SQSTM1 (Fig. 6L, M and Fig. S5A, B). To further validate the specificity of the HEP14's effects, we utilized PKC-specific siRNA to knockdown PKC in senescent KGN cells. The results obtained were consistent with those observed when PKC and ERK1/2 inhibitors were applied. Specifically, the reduction in PKC levels led to decreased phosphorylation of both PKC and ERK1/2, as well as decreased expression of downstream genes VDAC1, PINK1 (Fig. 6N and Fig. S5C), CAT, and TXNL1 (Fig. 6O and Fig. S5D). Conversely, there was an accumulation of MAP1LC3 and SQSTM1 (Fig. 6N and Fig. S5C). Importantly, these decreases induced by PKC-specific siRNA could not be rescued by HEP14 (Fig. 6N, O and Fig. S5C, D). These findings solidified the specificity of the HEP14's actions on PKC and ERK1/2 and downstream signal pathway. They provided robust support for the hypothesis that HEP14 enhances mitophagy via activation of the PKC-ERK1/2 signaling pathway. Collectively, the results underscore the pivotal role of the HEP14-activated PKC-ERK1/2 pathway in revitalizing mitophagy and mitochondrial function, thereby mitigating oxidative stress in senescent KGN cells.

HEP14 promoted ovarian follicle regeneration through the improvement of the ovarian micronenvironment in aged ovaries

To further determine the potential of HEP14 in promoting follicular regeneration and rejuvenating ovarian function in aged mice, a comprehensive histopathological examination was conducted following HEP14 treatment. Strikingly, the absolute size of aged ovaries treated with HEP14 exhibited significant increases compared to the control ovaries, similar to those of adult ovaries (Fig. 7A; Fig. S6A). Further Hematoxylin and Eosin (H&E) staining of HEP14-treated ovaries did not reveal any pathogenic changes in proliferation (Fig. S6A). Picosirius Red (PSR) staining revealed a remarkable reduction in fibrillar collagen deposition in the HEP14-treated ovaries (Fig. 7B). This was accompanied by downregulation of fibrosis marker α -smooth muscle actin (α -SMA)³³ (Fig. 7C) and senescent marker Galactosidase Beta 1 (Glb1)^{34,35} (Fig. S6B). Additionally, HEP14 treatment increased angiogenic markers Vascular Endothelial Growth Factor D (Vegfd)³⁶ and Platelet endothelial cell adhesion molecule-1 (PECAM-1/CD31)³⁷ (Fig. 7D; Fig. S6C). Together, these findings suggested the anti-fibrotic and pro-angiogenic effects of HEP14 to facilitate a more conducive microenvironment for ovarian cell regeneration.

A detailed quantification of follicles revealed that HEP14 treatment led to a marked increase in the number of primordial, pre-antral, antral follicles and corpus luteum compared to those in the controls (Fig. 7E, F). In agreement with these observations, Ki67 and Tunnel co-staining demonstrated a significant increase in Ki67-positive but Tunnel-negative follicles in the HEP14-treated ovaries, indicating increased cellular proliferation and reduced apoptosis (Fig. S6D). The latter result was supported by IHC staining revealing markedly downregulated expression of pro-apoptotic markers Bcl-2-associated X protein (Bax) and Cytochrome C (Cyto C) (Fig. S6E, F). RNA-seq data supported our histological observations, showing that 21 critical DEGs associated with follicle development and estrogen production, were restored to levels close to those in adult ovaries (Fig. 7G, H). IHC staining of ovarian sections validated a significant increase in the expression of Stanniocalcin-1 (Stc1), Estrogen receptor 1 (ESR1), Anti-Mullerian hormone receptor type 2 (Amhr2) - established markers of granulosa cells and Patched1 (Ptch1), a theca cell marker, as identified through RNA-seq analysis (Fig. 7I–L). Western blotting further confirmed a significantly increased expressions of Stc1, ESR1, and Amhr2 in HEP14-treated senescent KGN cells compared to those in control cells (Fig. 7M). However, this increase was abolished by PKC and ERK1/2 inhibitors, indicating that these signaling



molecules play a crucial role in mediating the effects of HEP14 (Fig. 7M). These results suggest that the HEP14-PKC-ERK1/2 signaling cascade is involved in the regeneration of follicular cells. Collectively, our findings comprehensively demonstrate that HEP14 promotes follicle regeneration in aged ovaries by fostering an optimal microenvironment through the activation of the HEP14-ERK1/2 signaling pathway.

HEP14 substantially restores ovarian endocrine function in aged mice

The endocrine function of the ovary is intrinsically linked to the ovarian follicle, where steroidogenesis relies on specialized mitochondrial enzymes within steroidogenic GCs. As shown in (Fig. 2K), HEP14 treatment of aged ovaries led to an enrichment in the expression of 20 key DEGs in pathway

Fig. 3 | Effect of HEP14-mediated mitophagy on oxidative stress within aged ovary. A Sub-heatmap data shows DEGs in the autophagy pathway. B mRNA expression levels of key DEGs from RNA-seq analysis in mitophagy pathway. C Representative images and expression levels of Map1lc3 and Sqstm1 by IF staining through double staining in ovarian sections. D Representative images and quantitative analysis of Map1lc3, Vdac1, and Lamp2 expression levels by IF through triple staining using the Manders' colocalization coefficients. E Sub-heatmap data shows DEGs in the pathway that is related to the oxidative stress response and F mRNA

levels of the selected DEGs from RNA-seq analysis. G Representative images and quantification of Cat, H Txnl1 and I Hmox1 expression levels by using IHC staining of ovarian sections. All data shows the comparison between HEP14-treated and vehicle-treated aged ovaries. Data are means \pm SEM, n = 4 biological replicates in (A, B) and (E, F), n = 3 biological replicates in (C, D) and (G–I). P values calculated by one-way ANOVA, followed by Turkey in (B, F); P values determined by unpaired two-tailed Student's t-test in (C, D) and (G–I). Changes were considered statistically significant when P < 0.05. Scale Bar, 100 μ m or 250 μ m.

“steroid hormone biosynthesis”, restoring to levels closely similar to those in adult ovaries (Fig. 8A, B). Among them, Stard4 and mitochondrial proteins Tspo, Vdac1, Hsd3b1 are essential for the transfer of cholesterol from the cytoplasm into the mitochondria. IHC staining and western blotting confirmed a significant increase in the protein levels of Vdac1 as shown in Figs. 3D, 6G, and Cyp1b1 (Fig. 8C, D) in HEP14-treated aged ovaries and senescent KGN cells treated with HEP14 respectively compared to their respective controls. Importantly, ELISA assays measuring ovarian gonadal hormone secretion revealed marked increases in E2, Amh and Inhibin A and B levels, along with a decrease in FSH levels in HEP14-treated aged mice compared to their counterparts (Fig. 8E). These hormonal changes suggest an improvement in endocrine function of the aged ovaries. Estrous cycle detection indicated that HEP14-treated aged mice exhibited recovered estrous cycles after 4 weeks of treatment, contrasting with the irregular cycles observed in control mice (Fig. 8F). To summarize, HEP14 demonstrates promise in enhancing hormone production and improving the endocrine function of aged ovaries, thereby laying a solid foundation for exploring its therapeutic potential in addressing age-related ovarian decline.

Discussion

Ovarian aging significantly affects reproductive health and plays a crucial role in the overall physiological aging of the body³⁸. Understanding the mechanisms driving this process is essential for the development of effective therapies to mitigate or potentially reverse age-related ovarian decline³⁹. Although recent research has largely focused on mitochondrial dysfunction as a key contributor to aging, our understanding of ovarian aging remains limited⁴⁰. In this study, we present the first evidence that HEP14 restores ovarian function in aged mice by activating the PKC-ERK1/2-mitophagy signaling cascade. This cascade enhances mitochondrial function, reduces oxidative stress, and promotes ovarian regeneration and functional recovery. This, in turn, promotes ovarian regeneration and the restoration of ovarian function.

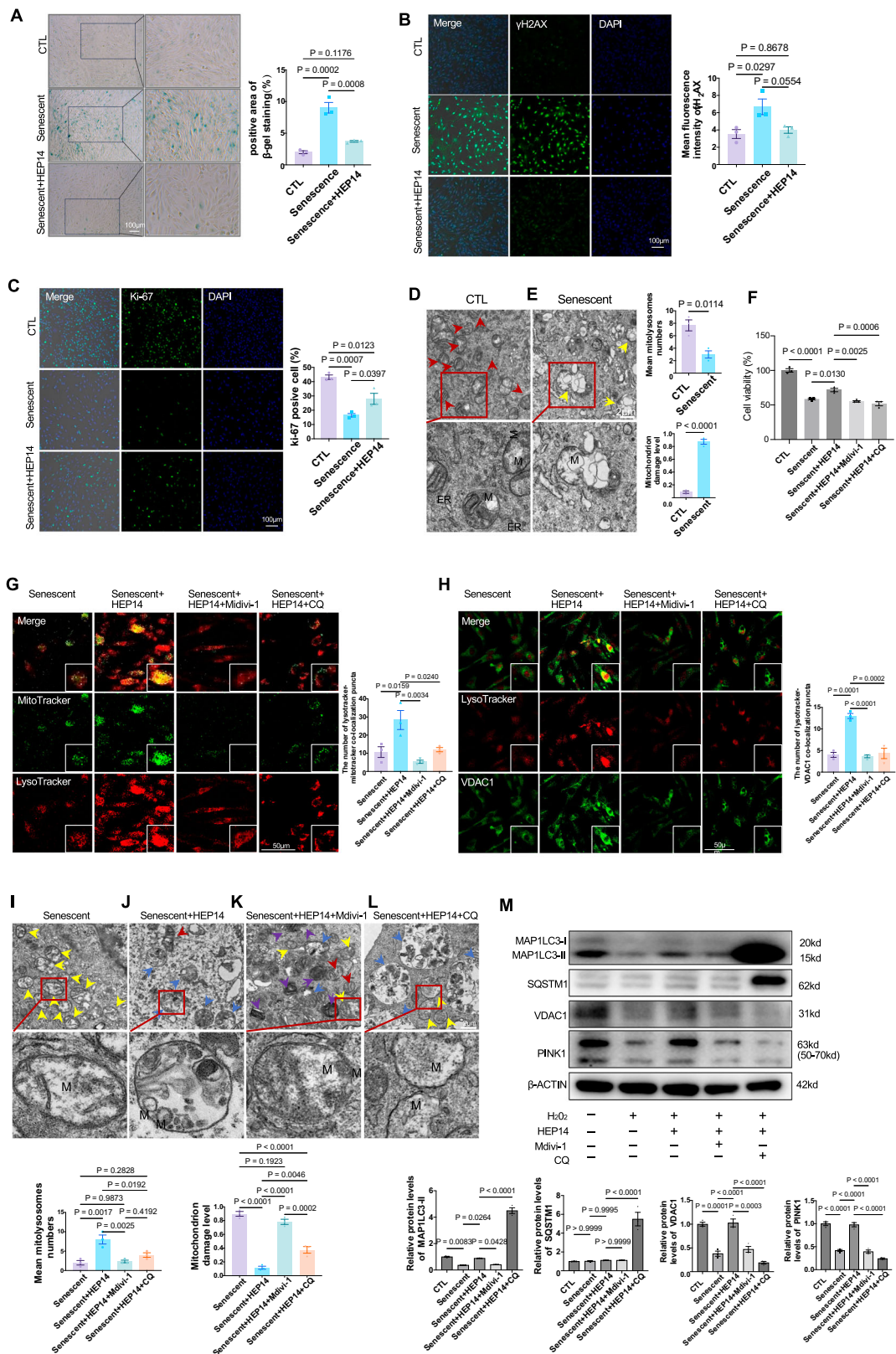
In the quest to unravel the anti-aging effects and underlying mechanisms of HEP14, we successfully developed HEP14/PLGA microspheres as a delivery system for this therapeutic agent. PLGA, a biodegradable copolymer with exceptional drug-loading properties^{41,42}, is extensively applied due to its safety, manipulable biodegradation rate^{43,44}, and has been approved by the Food and Drug Administration (FDA)⁴⁵, making it an ideal foundation for this delivery system. The HEP14/PLGA microspheres were meticulously optimized to ensure controlled and sustained release of HEP14 as indicated in Fig. 1A–E. The pivotal factors contributing to this sustained release include the successful encapsulation of HEP14 within the PLGA matrix, the alteration of HEP14's physical state within the microspheres, and the attainment of uniform size and shape for both the PLGA and HEP14/PLGA microspheres. Our findings corroborate with those reported by other authors^{42,45,46}. Ultimately, the innovative fabrication technique utilized for the HEP14/PLGA microspheres markedly enhances the therapeutic effectiveness of HEP14 in anti-aging treatments, representing a advancement in the field.

The comparative analysis of transcriptome in ovaries from vehicle-treated young, adult, and aged mice, as well as those from HEP14-treated adult and aged mice, revealed a significant overlap in the transcriptional profiles of HEP14-treated aged ovaries and those of adult ovaries. This indicates a remarkable similarity in their transcriptional patterns, suggesting a rejuvenation of aged ovaries at the genomic level following HEP14 intervention. The DEGs in HEP14-treated ovaries were enriched in the

signal pathways such as “autophagy”, “oxidative stress response”, “regulation of steroid hormone biosynthetic process” and “protein kinase C binding”. Among them, substantial and significant DEGs were mitophagy-related genes, as indicated in Fig. 3A. Mitophagy is a specific type of autophagy that targets and degrades damaged mitochondria. In the context of ovarian aging, the decline in mitophagy efficiency may exacerbate oxidative stress-induced damage, disrupt the ovarian microenvironment, affect hormone production and follicle development, ultimately leading to a further decline in ovarian function. Conversely, enhancing these degradation processes may help to mitigate oxidative stress and delay ovarian aging^{5,7,9,47}. This conclusion is supported by further in vitro and in vivo studies presented below. The regulation of PKC pathway is a recognized mechanism of physiologically changing cells⁴⁸. However, its specific role in the regulation of mitophagy, especially in the context of ovarian aging remains underexplored.

Follicle atresia is a tightly regulated process, hallmark by an initial rapid decline in GCs, followed by a gradual reduction in thecal cells. Age-related mitochondrial dysfunction in these cells reflect ovarian degeneration and abnormalities^{49,50}. Despite extensive research, the mechanisms underlying granulosa cell senescence remain largely unknown. Ovarian GCs play a pivotal role in steroidogenesis and follicle development, processes that are heavily reliant on mitochondrial integrity^{51,52}. Our in vitro studies have demonstrated that HEP14 is capable of rejuvenating the viability of senescent KGN cells, a model that closely mirrors human ovarian GCs^{15,53}. This rejuvenation is significantly attenuated by specific inhibitors that target mitophagy, lysosomes, PKC, and ERK1/2, highlighting the central role of PKC-ERK1/2-mitophagy cascades in the rejuvenating effects of HEP14. The increased colocalization of MitoTracker and Lysotracker, coupled with the increased expression of mitophagy-related proteins, indicated that HEP14 promoted mitophagy. This process is further confirmed by TEM assay, which is the gold standard for detection of formation of mitophagosome/mitolysosomes⁵⁴. Western blot analysis, in conjunction with pharmacological inhibitors and PKC-specific siRNA, provided further evidence that the HEP14-induced PKC-ERK1/2 signaling pathway effectively promoted mitophagy. Collectively, our findings demonstrated that HEP14 enhanced mitophagy in senescent KGN cells through the activation of the PKC-ERK1/2 signaling cascade. No prior studies have reported on the role of the PKC-ERK1/2-mitophagy signaling pathway activated by HEP14 in aged ovarian cells. Furthermore, HEP14 significantly improved mitochondrial function, as evidenced by an elevated $\Delta\Psi_m$ and a substantial reduction in ROS production within the mitochondria, which has been demonstrated to be associated with steroidogenic capacity of GCs⁵⁵. HEP14 also upregulated antioxidant genes such as CAT and TXNL1, which are responsible for scavenging excessive intracellular ROS. This process creates a favorable microenvironment for cell regrowth, as reported by others^{50–53}. Thus, HEP14's promotion of mitophagy enhances mitochondrial function and reduce oxidative stress in the senescent GCs. KGN cells express FSHR and show robust steroidogenic capacity upon FSH stimulation^{15,53}. These characteristics make KGN cells a suitable model for assessing the therapeutic effects of HEP14 on ovarian endocrine function in aged mice. It should be noted that differences in senescence response and apoptosis to H₂O₂ induction may exist between KGN cells and primary granulosa cells. Future studies should systematically validate these differences in this area.

Our in vivo results revealed that HEP14 treatment significantly increased the protein levels of key autophagy and mitophagy markers Map1lc3, Sqstm1, Vdac1, Pink1, lysosome marker Lamp2 as well as



phosphorylation levels of phosphorylated PKC and ERK/2. These findings were consistent with the RNA-seq data and in vitro results, provide a molecular basis for the enhancement of mitophagy in the HEP14-treated ovaries. The colocalization of Vdac1 signals with Map1lc3 and Lamp2 as well as Map1lc3 and Sqstm1 in HEP14-treated aged ovaries substantiated the role of HEP14 in strengthening mitophagy. Mitophagy has been

indicated for the removal of damaged mitochondria⁵⁶⁻⁵⁸. These discoveries imply that HEP14 facilitated the clearance of damaged mitochondria in the aged ovaries. Restoring mitochondrial function is crucial in aging ovaries, given that mitochondria are the main source of cellular ROS and are susceptible to ROS-induced damage⁵. As female age advances, antioxidant levels in the ovaries decline, which correlates with

Fig. 4 | Role of HEP14 on mitophagy in the H₂O₂-induced senescent KGN cells. **A** Increased percentages of SA- β -gal-positive cells by SA- β -gal staining. **B** Representative images of enhanced protein levels of γ H2A.X and **C** reduced protein levels of Ki67 by IF staining. **D** Representative TEM images and quantification of mitochondria, and **E** following H₂O₂ treatments, where red arrows indicate mitochondria, yellow arrows point to vacuolized mitochondria. **F** Viability of senescent KGN cells following HEP14 treatment alone or combined with Mitophagy inhibitor Mdivi-1 or lysosomal inhibitor CQ by CCK assays. **G** Representative fluorescence images and quantification of overlapped MitoTracker (green) and Lysotracker signals (red). **H** Representative fluorescence images and quantification of overlapped Lysotracker signals (red) and VDAC1 protein signals (green) by IF staining. **I** Representative TEM images and quantification of mitochondria, and mitolysosomes post treatment with **(J)** HEP14 alone or in combination with either

(K) mitophagy inhibitor Mdivi-1 or L lysosome inhibitor CQ. Yellow, red, purple and blue arrows indicate vacuolized mitochondria, mitochondria with regular morphology, residual mitochondrial myeloid bodies and mitolysosomes, respectively. **M** Protein levels of MAP1LC3, SQSTM1, VDAC1 and PINK1 post treatments with either Mdivi-1 or lysosomal inhibitor CQ by western blotting and densitometric analysis. All data show the comparison between senescent KGN cells and control cells treated with or without pharmacological treatment(s). Data are means \pm SEM, n = 3 in (A–M). P values calculated by one-way ANOVA, followed by Turkey-Kramer test except for (D, E) determined by unpaired two-tailed Student's t-test. Experiments were performed three times. Changes were considered statistically significant when P < 0.05. Scale Bar, 100 μ m except for TEM images, Scale Bar, 2 μ m.

notable age-related alterations in oxidatively damaged granulosa and theca cells within ovarian follicles. Oxidative stress is a key factor in this process as the ovary is particularly sensitive to ROS-induced damage due to its high metabolic activity and rich blood supply^{38,50,59}. Our RNA-seq analysis further suggested that HEP14 treatment restored the mRNA levels of 43 DEGs linked to the oxidative stress response, bringing them close to the levels observed in adult ovaries. IHC staining of ovarian sections confirmed significant increases in protein level of key antioxidant genes Cat, Txnll and Hmox1^{59–61}. These results demonstrated the anti-oxidative effects of HEP14 in aged ovaries, indicating an improved regrowth microenvironment following HEP14 treatment. Collectively, these results position HEP14 as a promising candidate for therapeutic intervention in age-related ovarian decline, potentially through modulation of mitophagy and antioxidant defense mechanisms.

Histopathological analysis of HEP14-treated aged ovaries showed significantly increased ovarian weight, indicating enhanced regeneration and follicular development. HEP14 exhibited anti-fibrotic and pro-angiogenic effects, creating a conducive environment for follicular regrowth^{33,36,37}. HEP14 treatment led to a quantifiable rise in follicles at various stages, with more Ki67-positive and fewer TUNEL-positive follicles, suggesting proliferation and reduced apoptosis. RNA-sequencing validated these findings, revealing upregulation of 21 key genes involved in follicle development. IHC and western blot analysis confirmed increased expression of Stc1, Esr1, Amhr2, and Ptch1, and decreased Bax and Cyto C. Stc1 promotes granulosa cell proliferation and steroid hormone synthesis^{62–65}, while ESR1 and Amhr2 are receptors for estrogen and AMH^{66,67}, respectively. Ptch1 is an early marker for theca cell differentiation⁶⁸. Reduced Bax and Cyto C indicate decreased apoptosis⁶⁹. The proliferation and apoptosis of GCs are closely related to ovarian regeneration and function^{70,71}. Altogether, these results suggest HEP14-enhanced mitophagy restores ovarian follicular regeneration and development by improving the ovarian microenvironment.

The ovary's steroid hormone synthesis capacity is tightly linked to follicular vitality, with GC mitochondria playing a crucial role²⁹. GSEA analysis showed upregulated pathways related to steroid hormone biosynthesis after HEP14 treatment, suggesting revitalized ovarian steroidogenic function. Key DEGs like Stard4, and mitochondrial proteins Tspo, Vdac1, Hsd3b1, and Cyp1b1 were upregulated, critical for steroid hormone production^{29,51}. Increased protein levels of Vdac1 and Cyp1b1, confirmed by IHC and western blot, supported enhanced steroidogenic potential in HEP14-treated aged ovaries. Physiologically, this manifested as elevated estradiol, AMH, and Inhibin B levels, with reduced FSH levels in HEP14-treated aged mice. The inverse correlation between FSH and Inhibin B indicated improved endocrine function and ovarian rejuvenation^{72,73}, supporting better reproductive health and potentially benefiting other physiological processes^{74,75}. Taken together, HEP14 treatment substantially restored ovarian endocrine function in aged mice.

In conclusion, our study provides new insight into the action mechanism of HEP14 in the context of ovarian aging. By precisely targeting the PKC-ERK1/2 signaling pathway, HEP14 effectively enhances mitophagy and reduces oxidative stress in ovarian cells. This targeted

action highlights HEP14's potential to rejuvenate aged ovarian function, as evidenced by the promotion of follicular regeneration and the restoration of endocrine balance. Furthermore, successful fabrication of HEP14/PLGA microspheres, as illustrated in the schematic diagram (Fig. 9), paves the way for innovative therapeutic strategies to combat ovarian aging and its associated reproductive and aging-related health issues.

Materials and methods

Mice and treatments

C57BL/6N mice were procured from GemPharmatech Co., LTD (Jiangshu, China) and maintained under specific pathogen-free (SPF) conditions, with temperature control (22 \pm 1 °C) and humidity control (60 \pm 10%) on a 12 h light/12 h dark cycle and ad libitum access to water and regular rodent chow. We have complied with all relevant ethical regulations for animal use. All animal procedures were approved by the Shenzhen Peking University-Hong Kong University of Science and Technology Medical Center's Animal Care and Use Committee in China (Protocol number: 2023-147) and were conducted in accordance with the National Laboratory Animal Care and Use research committee guidelines. Female mice were randomly divided into five groups: young (7–8 weeks, n = 6), adult (27–28 weeks, n = 6), aged (73–74 weeks, n = 8) mice treated with saline as controls, as well as adult mice (n = 6) and aged mice (n = 8) treated with HEP14/PLGA microspheres dissolved in saline at a dosage of 10 mg per kg of body weight (termed "Adult+HEP14 mice and Aged+HEP14 mice", respectively). Mice included in the young and adult groups were selected to be in the diestrous phase. The latter two groups received intraperitoneal injections every 5 days for a consecutive period of 30 days. After treatments, blood samples were collected from the retro-orbital plexus under 2% isoflurane; mice were then euthanized (cervical dislocation) and ovaries harvested for analysis.

Chemicals

HEP14 (5 β -O-angelate-20-deoxyingenol) was derived from *Euphorbia peplus* Linn plants by Professor Xiaojiang Hao's group¹² and dissolved in DMSO at a stock concentration of 25 mM. The PKC inhibitor, Go6850 (Bis1, Beyotime), was dissolved in DMSO at a stock concentration of 10 mM. The ERK inhibitor U0126 (Beyotime), was dissolved in DMSO at a stock concentration of 10 mg/ml. The mitophagy inhibitor Mdivi-1 (Selleck), was dissolved in DMSO at a stock concentration of 10 mM. The autophagy inhibitor Chloroquine (CQ, Selleck) was dissolved in DMSO at a stock concentration of 100 mM.

Preparation and characterization of HEP14/PLGA

HEP14/PLGA microspheres were synthesized by single emulsion solvent evaporation technique. The solution of PLGA (R-P0002-50k, Xi'an ruixin biological technology company) and HEP14 was dissolved in dichloromethane in a dark environment with magnetic stirring (400 rpm) at 5:1. The solution was added to 1% (w/v) polyvinyl alcohol (PVA, Macklin) aqueous solution, and the dichloromethanes were volatilized by magnetic stirring (300 rpm) at 25 °C for 12 h, and the microspheres were collected

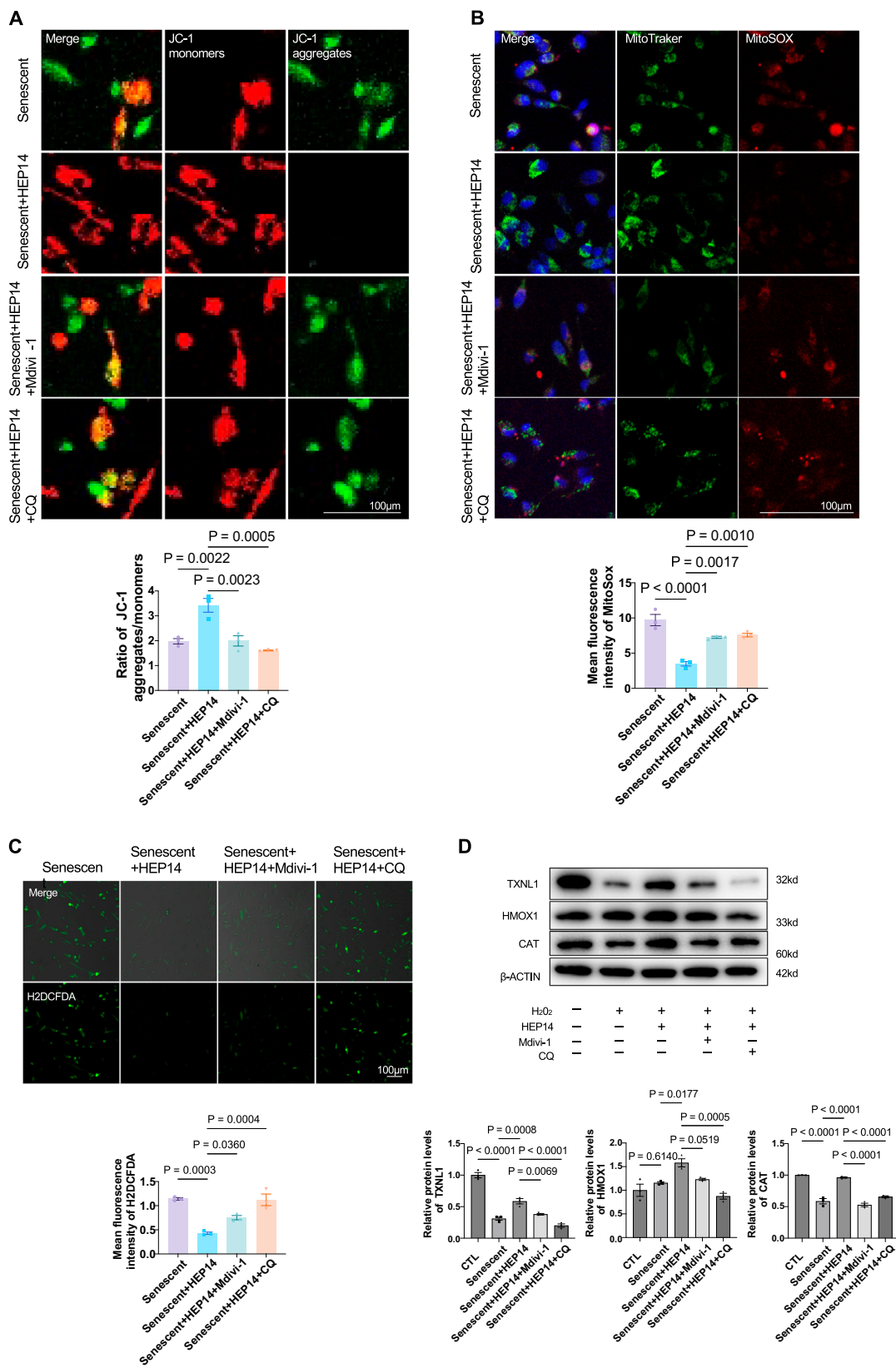
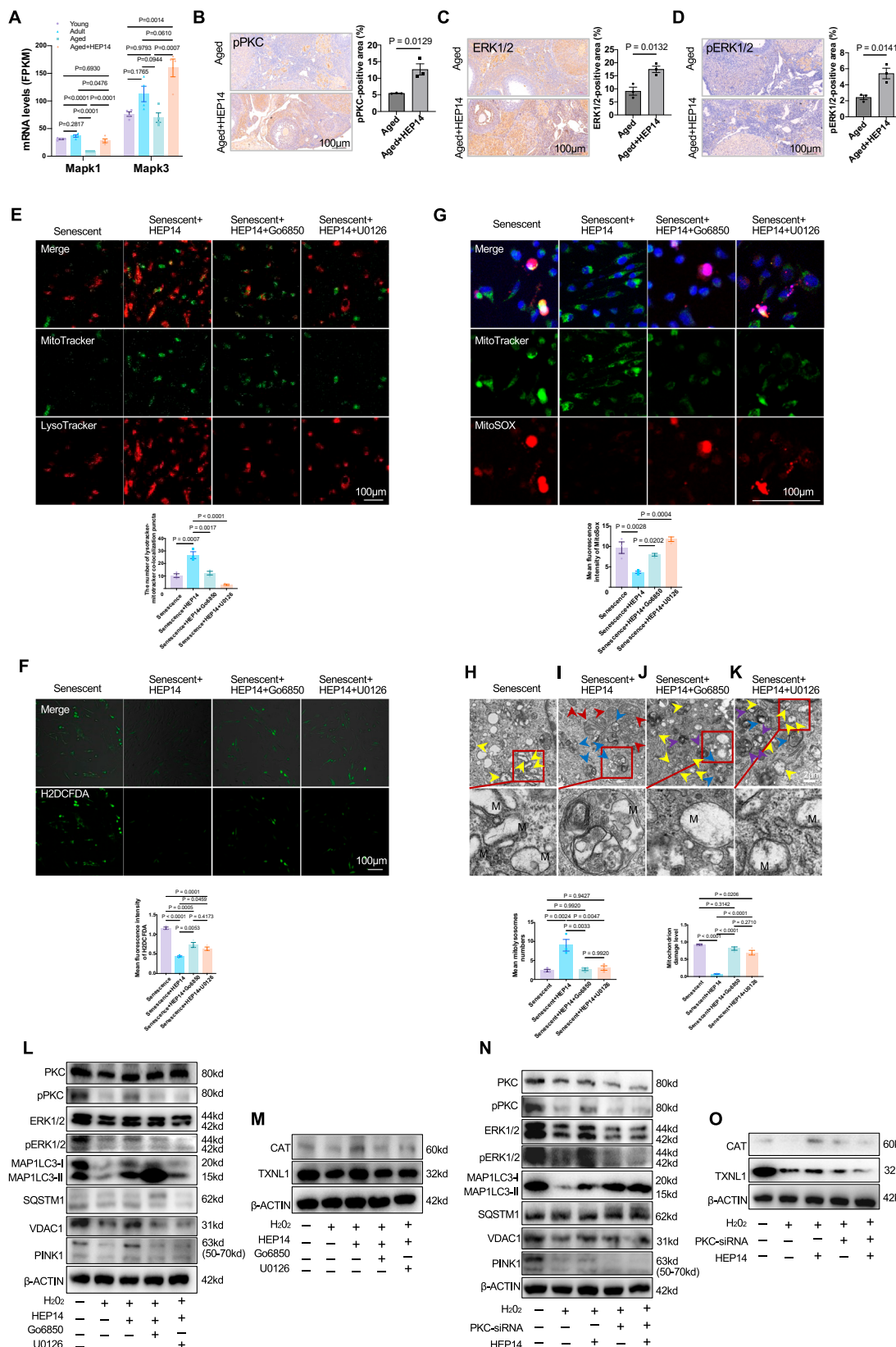


Fig. 5 | Impact of HEP14-enhanced mitophagy on mitochondrial function to clear ROS. A Representative images and quantification of mitochondrial membrane potential ($\Delta\Psi_m$) levels detected by JC-1 staining (red, high $\Delta\Psi_m$; green, low $\Delta\Psi_m$). B Representative fluorescence images and quantification of ROS levels obtained by co-staining with MitoTracker and MitoSOx, as well as (C) staining with H2DCFDA. D Protein levels of the key antioxidant genes CAT and TXNL1 by western blotting

and densitometric analysis. A–D show the comparison between HEP14-treated senescent KGN cells and vehicle-treated senescent KGN cells coupled with/without mitophagy inhibitor Mdivi-1 and lysosome inhibitor CQ. Data are means \pm SEM, $n = 3$ in (A–D). P values calculated by one-way ANOVA, followed by Tukey-Kramer test. Experiments were performed three times. Changes were considered statistically significant when $P < 0.05$. Scale Bar, 100 μ m.



after centrifugation (2000 × g, 5 min). After repeated rinsing of microspheres with distilled water to eliminate residual PVA, the microspheres were freeze-dried in a freeze-dryer for 24 h. PLGA microspheres can be prepared by the same methods. SEM (SU8100, HITACHI) was used to detect samples at the same scale, using ImageJ and Origin for particle size

analysis. The FTIR system (Vertex 70 v, Bruker) was used to characterize the sample with a scan range of 400–4000 cm⁻¹, a resolution of 4 cm⁻¹, a scan speed of 64 times/min, and a total of 1867 data points were generated. The X-ray diffraction (XRD) patterns of the samples were collected by Rigaku Smartlab X-ray diffractometer. Cu K α radiation (45 kV, 120 mA), 2 θ range

Fig. 6 | PKC-ERK1/2 signaling pathway is essential for HEP14-enhanced mitophagy signal cascades. A ERK1/2 mRNA levels from RNA-seq analysis, and B–D Representative images and quantification of pPKC, ERK1/2 and pERK1/2 in the HEP14-treated aged ovaries compared with vehicle-treated aged ovaries with IHC staining. E Representative fluorescence images and quantification of increased numbers of mitolysosome stained with MitoTracker green and Lysotracker red staining. F Representative fluorescence images and quantification by MitoTracker and MitoSox co-staining and G by H2DCFDA staining. H–K Representative TEM images and quantification of increased numbers of mitolysosomes and mitochondria by HEP14 induction, which were largely suppressed by PKC inhibitor Go6850 and ERK1/2 inhibitor U0126. Yellow, red, purple and blue arrows indicate vacuolized mitochondria, mitochondria with regular morphology, residual mitochondrial myeloid bodies and mitolysosomes, respectively. L Protein levels of PKC, pPKC, ERK1/2, pERK1/2, MAP1LC3, SQSTM1, VDAC1 and PINK1 and M CAT and TXNL1 by western blotting and densitometric analysis. N Protein levels of PKC, pPKC, ERK1/2, pERK1/2, VDAC1 and PINK1 and O CAT and TXNL1 by western blotting and densitometric analysis in KGN cells with PKC knockdown by siRNA. A–D show the comparison between HEP14-treated and vehicle-treated aged ovaries; E–O show the comparison between HEP14-treated senescent KGN cells and vehicle-treated senescent KGN cells coupled with/without PKC inhibitor Go6850 and ERK1/2 inhibitor U0126. Data are means \pm SEM, n = 4 biological replicates in (A), n = 3 biological replicates in (B–D), n = 3 in (E–O). P values calculated by one-way ANOVA, followed by Turkey-Kramer test in (A) and (E–O). P values determined by unpaired two-tailed Student's t-test in (B–D). Experiments were performed three times. Changes were considered statistically significant when P < 0.05. Scale Bar, 100 μ m except for TEM images, Scale Bar, 2 μ m.

is 5–100 °C. The resulting data were collected with transmittance values (%) and processed by Origin software.

Determination of drug loading rate and encapsulation efficiency of HEP14/PLGA microspheres and in vitro release study

The drug loading rate and encapsulation efficiency of HEP14/PLGA microspheres and the maximum absorbance of HEP14-methanol standard solution (0, 1, 2, 4, 6, 8, 10 μ g/mL) were determined by an ultraviolet spectrophotometer (UV-2600, SHIMADZU), and the standard curve of OD value (Y) and concentration (c) was drawn. The detection wavelength employed was 201 nm, and the sample size utilized was 1 mL. The drug load (%) and encapsulation efficiency (%) were calculated using the respective formulas below, where the theoretical drug load of microspheres refers to the initial amount of drug used for the preparation of microspheres. Drug loading (%) = (weight of drugs in microspheres)/(weight of microspheres) \times 100%; Entrapment efficiency (%) = (Actual drug load in the microsphere)/(Theoretical drug load of microspheres) \times 100%. The release rate of HEP14/PLGA microspheres in vitro was measured by an ultraviolet spectrophotometer (UV-2600, SHIMADZU) at 201 nm. PLGA/HEP14 microspheres were placed in PBS solution of pH 7.4, incubated at 37 °C and 100 rpm shaker, centrifuged (5000 \times g, 3 min) to precipitate microspheres, and collected the supernatant of 1, 3, 5, 7, 9, 11, 13, 15, 17, 19, 21 days.

KGN cell culture, KGN cell senescent model establishment and treatments

The granulosa cell line (KGN cells) was purchased from Shanghai Anwei Biotechnology Co., Ltd. (China). These KGN cells were cultured in a T25 culture flask using DMEM/F-12 medium (Gibco) supplemented with 10% fetal bovine serum (Gibco), 1% Glumax (Gibco), 1% NEAA (Gibco), and 1% penicillin/streptomycin (Gibco) at 37 °C in a humidified incubator with 5% CO₂. Once the cell density reached 70–80%, the KGN cells were transferred to in 6-well plates at a density of 1.2 \times 10⁵ cells/well. After the cells adhered, they were exposed to various concentrations (0, 25, 50, 75, 100, 150, 200 and 400 μ M) of H₂O₂ (Wako Pure Chemical Industries) for 4 h. Following this treatment, cell survival rates and aging-related markers were assessed. The optimal concentration for subsequent experiments was determined to be 75 μ M, which led to significant differences in expression of aging-related markers compared to those in untreated controls. Senescent KGN cells were further treated with various drugs alone or in combination. Initially, all senescent cell groups were exposed to 75 μ M H₂O₂ for 4 h. Subsequently, each group received additional treatments: 2.5 μ M HEP14 alone or in combination with 10 μ M Go6850, 50 μ M U0126, 5 μ M Mdivi-1, or 20 μ M CQ for a further 12 h. The respective cell groups were designated as follows: Senescent, Senescent + HEP14, Senescent + HEP14 + Go6850, Senescent + HEP14 + U0126, Senescent + HEP14 + Mdivi-1, and Senescent + HEP14 + CQ. After these treatments, the cells were either used for staining procedures or harvested for the preparation of RNA and protein samples for subsequent experiments.

Cell viability assay for KGN cells

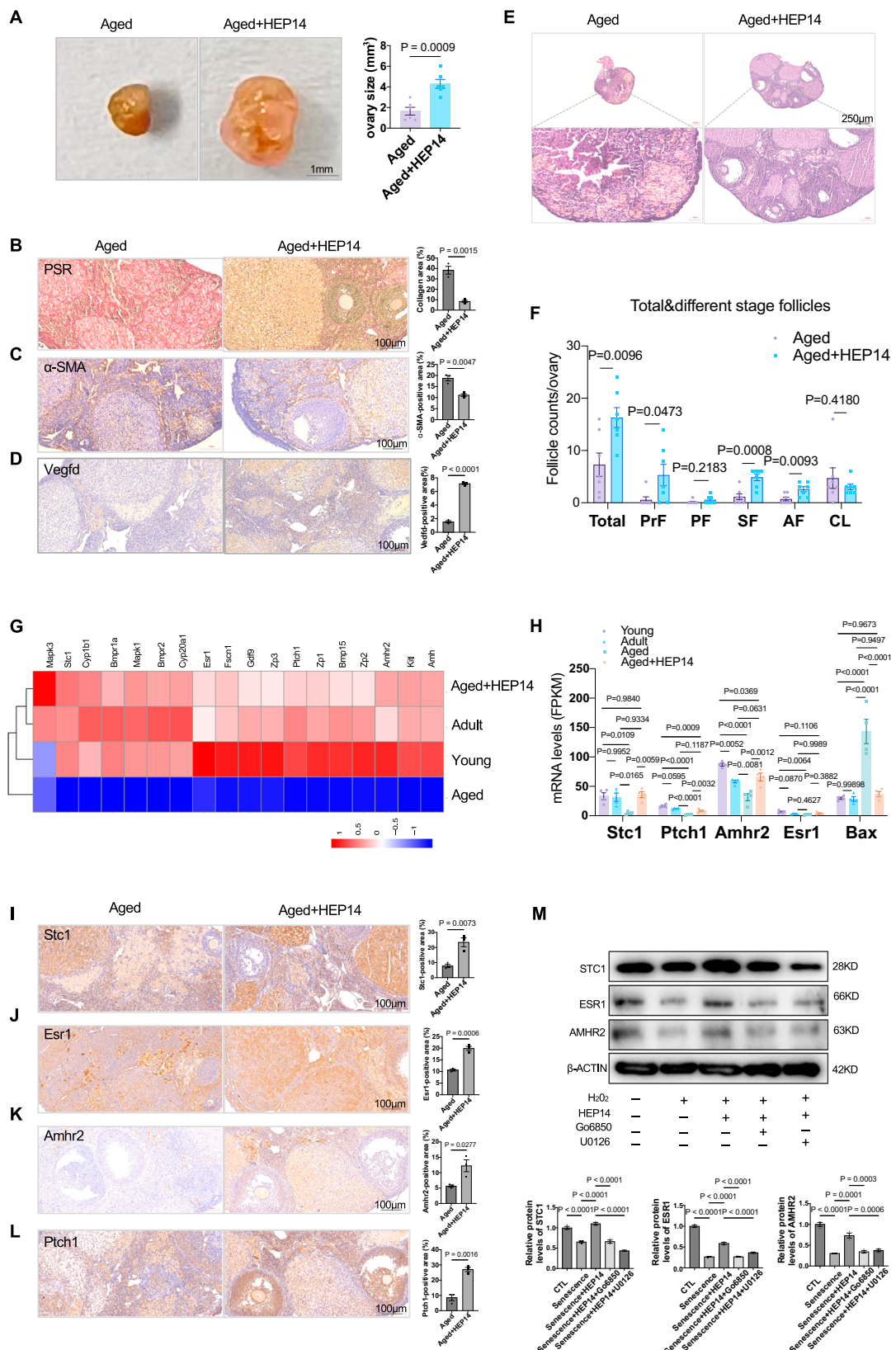
Cell viability was assessed using the Cell Counting Kit-8 (CCK8, MCE) assay. KGN cells were seeded in 96-well plates at a density of 6 \times 10³ cells/well. Following treatments with varying concentrations of H₂O₂ (0, 25, 50, 75, 100, 150, 200 and 400 μ M) for 4 h or different concentrations of HEP14 (0, 1.25, 2.5, 5 and 10 μ M) for 12, 24, or 48 h, 10 μ L of CCK-8 reagent (MCE) was added to each well. The plates were then incubated for 4 h at 37 °C. Subsequently, the absorbance was measured at 490 nm using a Microplate reader (Bio-Rad) to determine cell viability.

RNA-sequencing and functional enrichment analysis

Ovaries were carefully excised and washed three times with PBS to ensure cleanliness. Total RNA was then extracted from the ovarian tissue using TRIzol reagent according to the manufacturer's instructions (Invitrogen). Subsequently, RNA sequencing libraries were prepared with an insert size ranging from 370 to 420 bp. These libraries were sequenced on the Illumina NovaSeq 6000 platform (Novogene) to generate high-quality sequencing data. Prior to downstream analyses, the raw sequencing data underwent rigorous quality control to obtain clean reads. These clean reads were then mapped to the reference genome using the HISAT2 (v2.0.5) software, ensuring accurate alignment. Data processing and statistical analysis were performed using the powerful R programming language. To quantify gene expression levels, the featureCounts (v1.5.0-p3) tool was utilized to count the number of reads mapped to each gene. The Fragments Per Kilobase of transcript sequence per Million mapped reads (FPKM) value for each gene was calculated based on its length and the number of mapped reads. This metric provided a normalized measure of gene expression. Differential expression analysis was conducted between two groups, with two biological replicates per group, using the DESeq2 R HEP14kage (1.20.0). DESeq2 employs a model based on the negative binomial distribution to statistically determine differential expression in digital gene expression data. Genes were considered differentially expressed if they exhibited a $|\log_2 \text{fold change}| > 0$ and an adjusted p < 0.05. To gain insights into the functional roles of these differentially expressed genes, Gene Ontology (GO) analysis, encompassing biological processes, cellular components, and molecular functions, was performed. Both GO and KEGG analyses were carried out using the clusterProfiler R HEP14kage (3.8.1). Furthermore, gene set enrichment analysis (GSEA) was performed using GSEA v3.0.

Senescence-associated β -galactosidase staining

SA- β -gal staining kit (Beyotime) was used to stain and assess expression of senescence-associated β -galactosidase (SA- β -gal) in senescent KGN cells treated with varying concentrations of H₂O₂ using. KGN cells were seeded in a 6-well plate at a density of 1.2 \times 10⁵ cells/well. Once the cells reached 90% confluence, the medium was discarded, and the cells were rinsed once with PBS. Subsequently, the cells were fixed with 4% (w/v) paraformaldehyde for 15 min, followed by three additional rinses with PBS. Then, 1 mL of the working solution was added to each well, and the plate was incubated at 37 °C overnight in the dark. Senescent cells in each treatment group were observed under an optical microscope, and images were captured from three random fields of vision. Cell counting was performed using the ImageJ software (NIH).



PicoGreen assay for nucleic acid quantification

KGN cells were seeded in a 24-well plate at a density of 2.5×10^4 cells per well and subjected to different treatments. dsDNA was extracted from the cells in different groups following the protocol of the DNA Extraction and Purification Kits (Servicebio). Subsequently, the PicoGreen assay (Yeasen) was

used to quantify the concentration of dsDNA according to the manufacturer's instructions. Freshly prepared dsDNA Reagent working solution (consisting of 1 μ L dsDNA Reagent and 199 μ L of dsDNA Buffer) was added to each well of a 96-well plate at a volume of 190 μ L per well. Then, a gradient concentration of dsDNA standard or a sample to be tested was

Fig. 7 | The effects of HEP14 on ovarian regeneration in aged mice. A Ovarian weights of HEP14-treated aged ovaries compared to those in their counterparts. B Representative images and quantification of fibrillar collagen by PSR staining. C Protein expression level of α -SMA by IHC staining, and D Protein expression level of Vegf δ by IHC staining. E Representative images and F numbers of follicles at different developmental stages by H&E staining. PrF primordial follicle, PF primary follicle, SF secondary follicle, AF antral follicle, CL Corpus Luteum. G Sub-heatmap of DEGs associated to follicle development. H mRNA expression levels of key DEGs selected randomly from the RNA-seq analysis. I–L Representative images and quantification of Stc1, ESR1, Amhr2 and Ptch1 by IHC staining of ovarian sections.

All data show the comparisons between HEP14-treated aged and vehicle-treated ovaries. M Protein expression levels of Stc1, ESR1 and Amhr2 were confirmed by western blotting and densitometric analysis in the HEP14-treated senescent KGN cells compared to their control cells. Data are means \pm SEM, n = 6–8 biological replicates in (A, E), n = 3 biological replicates in (B–D) and (I–L), n = 4 biological replicates in (F–H), n = 3 in (M). P values determined by unpaired two-tailed Student's t-test in (A–F) and (I–L). P values calculated by one-way ANOVA, followed by Tukey-Kramer test in (H, M). Changes were considered statistically significant when $P < 0.05$. Scale Bar, 100 μ m or 250 μ m.

added to the plate at a volume of 10 μ l per well. dsDNA Standard 2 provided in the kit was used to establish a dsDNA stand and curve with corresponding concentrations. The fluorescence signal value was detected using a fluorescence microplate reader (Agilent BioTek Synergy H1), with the excitation wavelength (Ex) set to 480 nm and the emission wavelength (Em) set to 520 nm. The dsDNA concentration of the samples to be measured was determined by substituting the fluorescence signal value into the corresponding cell growth curve.

MitoTracker and Lysotracker staining

KGN cells were seeded in a 24-well plate at a density of 2.5×10^4 cells/well with different treatments were incubated with 200 nM MitoTracker green (Beyotime) and 50 nM Lysotracker red (Beyotime) diluted with DMEM/F12 medium (without FBS) for 30 min at 37 °C to specifically assess mitochondrial and lysosome numbers. Both green and red channels using excitation at 490 nm and emission at 516 nm (green signals) together with excitation at 577 nm and emission at 590 nm (red signals) under a laser scanning confocal microscope (Nikon).

Detection of ROS production

The level of Reactive Oxygen Species (ROS) was quantified using H2DCFDA (MCE) and MitoSox (Beyotime) detection probe, respectively. To ensure precise measurements, KGN cells undergoing different treatments were incubated with either 10 μ M H2DCFDA or 1 μ M MitoSox dissolved in FBS-free medium for 20 min at 37 °C. After incubation, the medium containing H2DCFDA or MitoSox was carefully removed, and the cells were thoroughly washed to eliminate any residual unconjugated probe. The ROS levels were then ascertained by evaluating the fluorescence intensity, excitation at 490 nm and emission at 516 nm for green signals, as well as excitation at 577 nm and emission at 590 nm for red signals under a laser scanning confocal microscope (Nikon).

Measurement of the mitochondrial membrane potential (MMP, $\Delta\Psi_m$)

Mitochondrial membrane potential (MMP, $\Delta\Psi_m$) was detected using a JC-1 staining kit (MCE) following the manufacturer's instruction. Cells were incubated with a 5 μ M JC-1 solution in serum-free medium at 37 °C in a dark setting for 30 min. After incubation, the cells were thoroughly washed with DPBS to eliminate residual dye. Imaging was promptly conducted using a laser scanning confocal microscope, simultaneously capturing both green and red fluorescence channels (excitation/emission at 488 nm/530 nm and 568 nm/590 nm, respectively). Fluorescence intensities in both channels were quantified using Image J software (NIH). A quantitative measurement of $\Delta\Psi_m$ expressed as the ratio of red to green fluorescence. This ratio reflects the mitochondrial membrane potential status within the cells.

Knockdown using siRNA

RNA oligonucleotides used for siRNA targeting PKC are: 5'-AUUU-GAAUGUAAGGACU CCTT-3', 5'-AGUAACAAAUCAUGGCAC TT-3' and 5'-AUUCAUACAACAGGACGCTT-3' (GenePharma). Cells were transfected with 100 pmol RNA oligonucleotides in 6-well plates using Lipofectamine 3000 (Thermo Scientific). The knockdown effect of siRNA was evaluated 48 h after transfection by western blotting.

Western blots

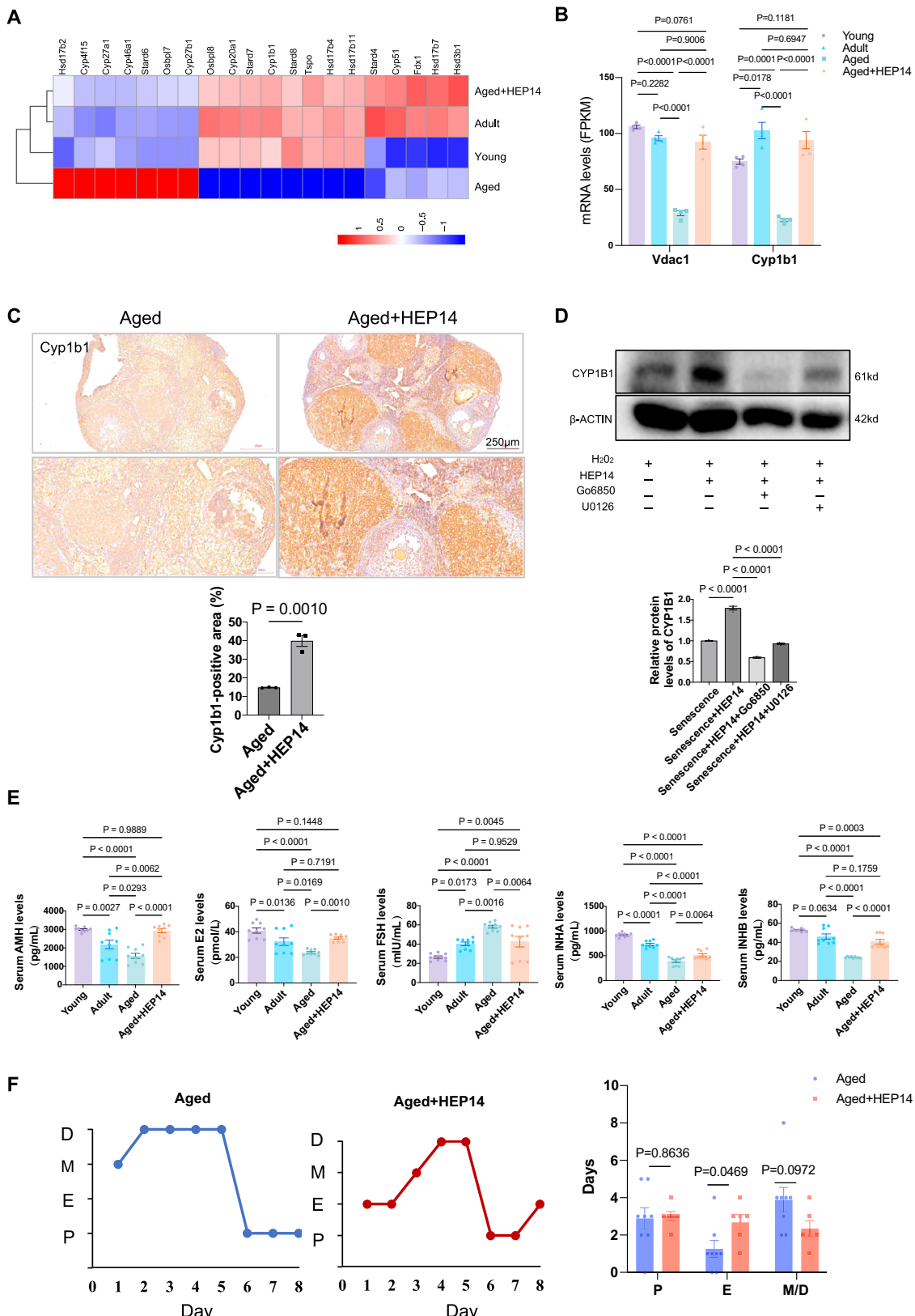
Cells were lysed using ice-cold RIPA buffer (Solarbio) supplemented with Complete Protease Inhibitor Cocktail (1 tablet dissolved in 50 ml) (Roche) and Phosphatase Inhibitor Cocktail (1 tablet dissolved in 10 ml) (Roche). The cell lysates were then cleared by centrifugation at 12,000 rpm for 15 min. Protein concentrations were determined using a BCA kit (Thermo Scientific). Subsequently, proteins were denatured at 98 °C for 5 min. Twenty micrograms of protein from each sample were separated using sodium dodecyl sulfate polyacrylamide gel electrophoresis (12% SDS-PAGE). The proteins were then transferred to PVDF membranes (Millipore) and blocked with blocking buffer for 1 h at room temperature. The membranes were incubated with various primary antibodies, including anti-LC3, anti-SQSTM1/p62, anti-TXNL1, anti-HO-1, anti-Cat, anti-PKC alpha, anti-pPKC alpha (Thr638), anti-ERK1/2, Anti-p44/42 MAPK (Erk1/2), anti-VDAC1, anti-ER alpha, anti-STC1, anti-AMHR2, anti-CYP1b1, and anti-ACTB/ β -actin. This was followed by incubation with HRP-conjugated secondary antibodies for 1 h. The target proteins were detected using an enhanced chemiluminescence (ECL) detection system (Bio-Rad). Blot signals were quantified using ImageJ software (NIH). All antibodies used in this study were listed in the Supplementary Tables S1 and S2.

Transmission electron microscopy

KGN cells were pre-fixed for 2 h at room temperature using an electron microscopy fixative from Servicebio. After washing in 100 mM phosphate buffer (composed of KH2/Na2HPO4 at pH 7.4), the cells underwent post-fixation with 1% osmium tetroxide (OSO4) for 60 min. Subsequent phosphate buffer washes preceded a dehydration process, gradually increasing the ethanol concentration from 30% to 100% in 15-min increments. This was followed by two 20-min incubations in 100% acetone. The infiltration process commenced with a 1:1 mixture of acetone and Spurr's resin for 2 h, progressing to a 1:2 mixture overnight at 37 °C. This was followed by incubations in pure Spurr's resin for 5 h and then for 48 h at 60 °C to ensure complete polymerization. The polymerized resin blocks were then sliced into ultra-thin sections (60–80 nm thick), mounted on nickel grids, and stained with 2% uranyl acetate for 10 min and 2.6% lead citrate for 5 min. These prepared sections were examined using a Hitachi HT7800 transmission electron microscope (TEM) at 80 kV.

Immunofluorescence (IF) staining

KGN cells were seeded onto glass coverslips placed in 12-well plates and cultured for 48 h. Subsequently, the cells were rinsed with PBS, fixed using 4% paraformaldehyde for 15 min at room temperature, and then permeabilized with 0.25% TritonX-100 for 10 min (Servicebio). To block non-specific binding sites, the slides were treated with 2% BSA dissolved in TBST (Servicebio) for 1 h. Following this, the slides were incubated overnight at 4 °C with primary antibodies targeting LC3, SQSTM1/p62, Ki67, and γ H2AX, diluted in 2% BSA in TBST. The slides were then washed thoroughly with TBST before being incubated with the corresponding secondary antibody, Goat anti-Rabbit IgG (FITC), and DAPI (Beyotime) for nuclear staining. Finally, the stained cells were observed under a fluorescent microscope (Leica). All antibodies used in this study are listed in the Supplementary Tables S1 and S2.



Hematoxylin-eosin staining of ovarian sections and follicle counts

The ovaries, collected at designated time points, were fixed in 4% paraformaldehyde (Solarbio) for a 24 h. After paraffin embedding, the ovarian tissues were sliced into 6 mm sections. From each ovary,

three consecutive sections with intervals of five were carefully chosen for hematoxylin-eosin (H&E) staining following the manufacturer's guidelines (Solarbio). The stained slices were imaged using the Glass slide scanning imaging system (SQS-1000, Teksquare). A detailed morphological analysis of each ovarian section was conducted,

Fig. 8 | The regulatory actions of HEP14 on ovarian endocrine function in aged mice. **A** Sub-heatmap of 20 DEGs enriched in the pathway of “regulation steroid hormone biosynthetic process” by GSEA. **B** mRNA expression levels of the key DEGs involved in the pathway indicated in RNA-seq analysis, and **C** Representative images and quantification of mitochondrial proteins Cyp1b1 by IHC staining of ovarian sections. The data presented in (A–C) are from the comparison of HEP14-treated aged ovaries with their counterparts. **D** Protein levels of Cyp1b1 in the HEP14-treated senescent KGN cells with their controls by western

blotting and densitometric analysis. **E** Serum levels of ovarian hormone E2, AMH, Inhibin A, Inhibin B and FSH by ELISA assays in the HEP14-treated aged mice in contrast to their counterparts. **F** Estrous cycles of HEP14-treated mice compared to those in the vehicle-treated controls. Data are means \pm SEM, $n = 4$ biological replicates in (A, B) and (E, F), $n = 3$ biological replicates in (C), $n = 3$ in (D). P values calculated by one-way ANOVA, followed by Turkey in (B) and (D, E); P values determined by unpaired two-tailed Student’s t-test in (C, F). Changes were considered statistically significant when $P < 0.05$. Scale Bar, 100 μ m or 250 μ m.

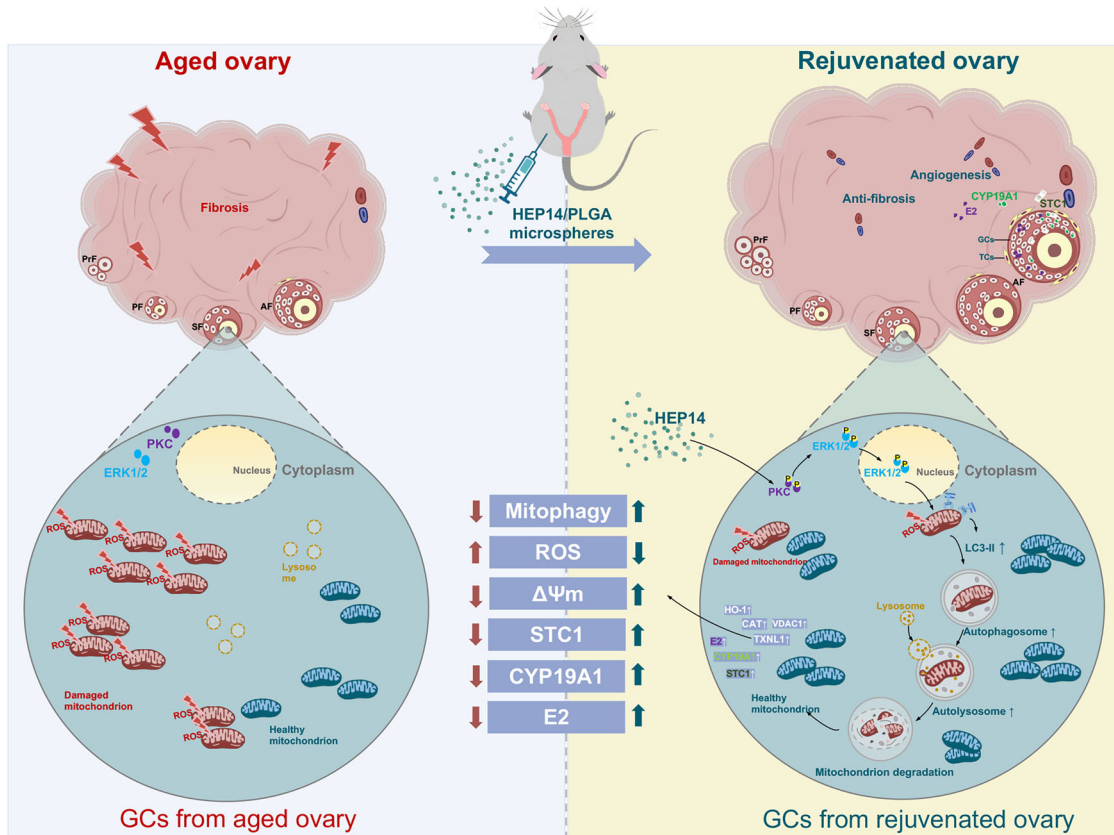


Fig. 9 | A diagram showing how HEP14 rejuvenates aged ovary by enhancing mitophagy via PKC-ERK1/2 pathway. GCs Granulosa Cells, TCs Theca Cells, PrF Primordial Follicles, PF Primary Follicles, SF Secondary Follicles, AF Antral Follicles.

and various stages of follicles including primordial, primary, secondary, antral, and atretic follicles, as well as the corpus luteum were counted.

TUNEL assay

Ovarian granulosa cell apoptosis was examined using a TUNEL assay kit (Servicebio) following the manufacturer’s instructions. Briefly, deparaffinized tissue sections were incubated with proteinase K (20 mg/mL) at 37 °C for 20 min, followed by incubation with permeabilization buffer at room temperature for 20 min. After equilibration at room temperature for 10 min, sections were incubated with terminal deoxynucleotidyl transferase and deoxyuridine triphosphate at 37 °C for 2 h in a moist chamber. Nuclei were counterstained with DAPI. Images were acquired using a Nikon Eclipse Ti-SR microscope.

Estrous cyclicity

Vaginal smears were performed at 9:00 am every morning for consecutive 4 weeks to examine the estrous cycle before and after treatment. First, cotton swabs were moistened with saline, rotated gently in the vagina, and then smeared on adhesive slides. Next, the detached cells were observed in microscope to determine the different stages of the estrous cycle, such as proestrus, estrus, metoestrus and diestrus.

Enzyme-linked immunosorbent assay (ELISA)

Blood samples were collected from the mice, and serum was separated by centrifuging at 5000 rpm for 10 min. The serum levels of anti-Müllerian hormone (AMH), estradiol (E2), follicle-stimulating hormone (FSH), Inhibin A (INH A), and Inhibin B (INH B) were determined. The ELISA kits for measuring E2, AMH, FSH, INH A and INH B were purchased from Meimian Industrial Co., Ltd (Jiangsu). The functional sensitivity of the assays was 0.1 pg/mL for E2, 11.75 pg/mL for AMH, and 0.1 mIU/mL for FSH. For INH A and INH B, the functional sensitivities were 1.0 pg/mL and 0.1 pg/mL, respectively. The absorbance was then measured at 450 nm using a microplate reader (Rayto). The concentrations of these hormones were subsequently calculated by referencing a standard curve.

Immunohistochemistry (IHC)

Paraffin-embedded ovarian sections were incubated with a range of primary antibodies including anti-LC3, anti-SQSTM1/p62, anti-TXNL1, anti-HO-1, anti-Cat, anti-pPKC alpha (Thr638), anti-ERK1/2, Anti-p44/42 MAPK (Erk1/2), anti-VDAC1, anti-ER alpha, anti-STC1, anti-AMH, and anti-CYP1b1, at 4 °C overnight. Following this, the slides were incubated with biotinylated secondary antibodies, namely HRP-labeled Goat anti-Rabbit IgG and HRP-labeled Goat anti-mouse IgG, at 37 °C for 30 min. Development was carried out using diaminobenzidine (DAB, Servicebio) as the

chromogen, and the sections were counterstained with hematoxylin. Images were captured using the Glass slide scanning imaging system (SQS-1000, Teksquare). ImageJ software (NIH) facilitated the analysis of staining results. All antibodies utilized in this study were listed in the Supplementary Tables S1 and S2.

Multiple immunofluorescence labeling staining

Paraffin-fixed ovarian sections were incubated with various primary antibodies such as anti-LC3, anti-SQSTM1/p62, anti-VDAC1, and anti-LAMP2, at 4 °C overnight. This was followed by incubation with the corresponding secondary antibodies: Goat anti-Rabbit IgG (Alexa Fluor 488), Goat anti-Rabbit IgG (CY3), and Goat anti-Rabbit IgG (CY5) at 37 °C for 1 h. Nuclei were stained with DAPI (Beyotime). The slides were then imaged using the Pannoramic MIDI scanner (3DHISTECH). During imaging, Alexa Fluor 488 emitted green fluorescence with an excitation wavelength of 465–495 nm and an emission wavelength of 515–555 nm. CY3 emitted pink fluorescence with an excitation wavelength of 532–554 nm and an emission wavelength of 576–596 nm. CY5 emitted pink fluorescence as well, but with an excitation wavelength of 608–648 nm and an emission wavelength of 672–712 nm. DAPI emitted blue fluorescence with an excitation wavelength of 330–380 nm and an emission wavelength of 420 nm, staining the nuclei blue under UV excitation. Positive expressions corresponded to fluorescence labeled in red and green. All antibodies used in this study were listed in the supplementary Tables S1 and S2.

Picosirius Red staining and fibrosis area quantification

Picosirius Red (PSR) staining kit (Solarbio) was used to stain collagen I/III according to the manufacturer's recommendations. Briefly, ovarian sections were first deparaffinized by immersing twice in xylene, once in 90% ethanol, 70% ethanol and 50% ethanol for 5 min each and then hydrated in water twice for 5 min each. After removing excess water, slides were immersed in hematoxylin for 10 min and then in PSR stain for 1 h after removing excess water. Following a quick wash twice with acetic acid and absolute ethanol, slides were rinsed with xylene and mounted with DPX mounting resin after removing excess xylene. Images were captured using Glass slide scanning imaging system (SQS-1000, Teksquare). For every mouse, fibrosis was measured in a single cross section of the entire ovary. The fibrotic area of imaged PSR-stained or collagen-immunolabeled ovaries was quantified using Image J software (NIH).

Statistics and reproducibility

Data were expressed as the mean \pm standard error (SEM) of the mean and analyzed using the GraphPad Prism 9.4.1 statistic software (GraphPad Software). Student's t test is used to compare the means between two groups. One-way ANOVA was used for the homogeneous variance in three or more group comparisons followed by the Tukey between groups. Welch's ANOVA was applied to the uneven variance in three or more group comparisons followed by Games-Howell method between groups. The sample sizes "n" refer to biologically independent samples/experiments, and the exact "n" values are indicated in the figure legends. A p value of <0.05 was considered to be a significant difference.

Reporting summary

Further information on research design is available in the Nature Portfolio Reporting Summary linked to this article.

Data availability

All data necessary to evaluate the conclusions in this paper are included in the manuscript and/or the Supplementary Materials. The RNA-sequencing data have been deposited in the Gene Expression Omnibus (GEO) database with the accession code GSE273724. Uncropped blot images are provided in Supplementary information as Fig. S7. Source data are provided in Supplementary Data 1 and 2. Any additional data related to this study can be requested from the corresponding authors upon reasonable request.

Received: 26 January 2025; Accepted: 22 July 2025;

Published online: 01 August 2025

References

- McGee, E. A. & Hsueh, A. J. Initial and cyclic recruitment of ovarian follicles. *Endocr. Rev.* **21**, 200–214 (2000).
- Tal, R. & Seifer, D. B. Ovarian reserve testing: a user's guide. *Am. J. Obstet. Gynecol.* **217**, 129–140 (2017).
- Broekmans, F. J., Knauff, E. A., te Velde, E. R., Macklon, N. S. & Fauer, B. C. Female reproductive ageing: current knowledge and future trends. *Trends Endocrinol. Metab.* **18**, 58–65 (2007).
- Broekmans, F. J., Soules, M. R. & Fauer, B. C. Ovarian aging: mechanisms and clinical consequences. *Endocr. Rev.* **30**, 465–493 (2009).
- Sasaki, H. et al. Impact of oxidative stress on age-associated decline in oocyte developmental competence. *Front. Endocrinol.* **10**, 811 (2019).
- Onishi, M., Yamano, K., Sato, M., Matsuda, N. & Okamoto, K. Molecular mechanisms and physiological functions of mitophagy. *EMBO J.* **40**, e104705 (2021).
- Smits, M. A. J. et al. Human ovarian aging is characterized by oxidative damage and mitochondrial dysfunction. *Hum. Reprod.* **38**, 2208–2220 (2023).
- Manabe, N. et al. Role of cell death ligand and receptor system on regulation of follicular atresia in pig ovaries. *Reprod. Domest. Anim.* **43**, 268–272 (2008).
- Alberico, H. C. & Woods, D. C. Role of granulosa cells in the aging ovarian landscape: a focus on mitochondrial and metabolic function. *Front. Physiol.* **12**, 800739 (2021).
- Liu, T., Huang, Y. & Lin, H. Estrogen disorders: interpreting the abnormal regulation of aromatase in granulosa cells (Review). *Int. J. Mol. Med.* **47**, <https://doi.org/10.3892/ijmm.2021.4906> (2021).
- Hoyer-Hansen, M. et al. Control of macroautophagy by calcium, calmodulin-dependent kinase kinase-beta, and Bcl-2. *Mol. Cell* **25**, 193–205 (2007).
- Li, Y. et al. Protein kinase C controls lysosome biogenesis independently of mTORC1. *Nat. Cell Biol.* **18**, 1065–1077 (2016).
- Denning, M. F., Dlugosz, A. A., Threadgill, D. W., Magnuson, T. & Yuspa, S. H. Activation of the epidermal growth factor receptor signal transduction pathway stimulates tyrosine phosphorylation of protein kinase C delta. *J. Biol. Chem.* **271**, 5325–5331 (1996).
- Detjen, K. M. et al. Activation of protein kinase Calpha inhibits growth of pancreatic cancer cells via p21(cip)-mediated G(1) arrest. *J. Cell Sci.* **113**, 3025–3035 (2000).
- Nishi, Y. et al. Establishment and characterization of a steroidogenic human granulosa-like tumor cell line, KGN, that expresses functional follicle-stimulating hormone receptor. *Endocrinology* **142**, 437–445 (2001).
- Zhuang, H., Ren, X., Zhang, Y., Li, H. & Zhou, P. β -Hydroxybutyrate enhances chondrocyte mitophagy and reduces cartilage degeneration in osteoarthritis via the HCAR2/AMPK/PINK1/Parkin pathway. *Aging Cell* **n/a**, e14294. <https://doi.org/10.1111/ace.14294> (2024).
- Liu, L. et al. The physiological metabolite α -ketoglutarate ameliorates osteoarthritis by regulating mitophagy and oxidative stress. *Redox Biol.* **62**, 102663 (2023).
- Yao, N. et al. Inhibition of PINK1/Parkin-dependent mitophagy sensitizes multidrug-resistant cancer cells to B5G1, a new betulinic acid analog. *Cell Death Dis.* **10**, 232 (2019).
- Zhang, Y. et al. Listeria hijacks host mitophagy through a novel mitophagy receptor to evade killing. *Nat. Immunol.* **20**, 433–446 (2019).
- Wu, Q. et al. Mdivi-1 alleviates blood-brain barrier disruption and cell death in experimental traumatic brain injury by mitigating autophagy

dysfunction and mitophagy activation. *Int J. Biochem. Cell Biol.* **94**, 44–55 (2018).

21. Sun, Y., Vashisht, A. A., Tchieu, J., Wohlschlegel, J. A. & Dreier, L. Voltage-dependent anion channels (VDACs) recruit Parkin to defective mitochondria to promote mitochondrial autophagy. *J. Biol. Chem.* **287**, 40652–40660 (2012).
22. Geisler, S. et al. PINK1/Parkin-mediated mitophagy is dependent on VDAC1 and p62/SQSTM1. *Nat. Cell Biol.* **12**, 119–131 (2010).
23. Messina, A., Reina, S., Guarino, F. & De Pinto, V. VDAC isoforms in mammals. *Biochim. Biophys. Acta* **1818**, 1466–1476 (2012).
24. Lynch-Day, M. A., Mao, K., Wang, K., Zhao, M. & Klionsky, D. J. The role of autophagy in Parkinson's disease. *Cold Spring Harb. Perspect. Med.* **2**, a009357 (2012).
25. Tooze, S. A. & Yoshimori, T. The origin of the autophagosomal membrane. *Nat. Cell Biol.* **12**, 831–835 (2010).
26. Eskelinen, E. L. Roles of LAMP-1 and LAMP-2 in lysosome biogenesis and autophagy. *Mol. Asp. Med.* **27**, 495–502 (2006).
27. Gough, N. R. & Fambrough, D. M. Different steady state subcellular distributions of the three splice variants of lysosome-associated membrane protein LAMP-2 are determined largely by the COOH-terminal amino acid residue. *J. Cell Biol.* **137**, 1161–1169 (1997).
28. Kaseder, M. et al. Evidence of a role for cAMP in mitochondrial regulation in ovarian granulosa cells. *Mol. Hum. Reprod.* **28**, <https://doi.org/10.1093/molehr/gaac030> (2022).
29. Sreerangaraja Urs, D. B. et al. Mitochondrial function in modulating human granulosa cell steroidogenesis and female fertility. *Int. J. Mol. Sci.* **21**, <https://doi.org/10.3390/ijms21103592> (2020).
30. Chakraborty, J., Caicci, F., Roy, M. & Ziviani, E. Investigating mitochondrial autophagy by routine transmission electron microscopy: seeing is believing?. *Pharm. Res.* **160**, 105097 (2020).
31. Kauffman, M. E. et al. MitoSOX-based flow cytometry for detecting mitochondrial ROS. *React. Oxyg. Species* **2**, 361–370 (2016).
32. Lyublinskaya, O. G. et al. Redox environment in stem and differentiated cells: a quantitative approach. *Redox Biol.* **12**, 758–769 (2017).
33. Briley, S. M. et al. Reproductive age-associated fibrosis in the stroma of the mammalian ovary. *Reproduction* **152**, 245–260 (2016).
34. Dimri, G. P. et al. A biomarker that identifies senescent human cells in culture and in aging skin in vivo. *Proc. Natl. Acad. Sci. USA* **92**, 9363–9367 (1995).
35. Sun, J. et al. A Glb1-2A-mCherry reporter monitors systemic aging and predicts lifespan in middle-aged mice. *Nat. Commun.* **13**, 7028 (2022).
36. Wang, P. et al. VEGF-induced angiogenesis ameliorates the memory impairment in APP transgenic mouse model of Alzheimer's disease. *Biochem. Biophys. Res. Commun.* **411**, 620–626 (2011).
37. Hohman, T. J., Bell, S. P. & Jefferson, A. L. The role of vascular endothelial growth factor in neurodegeneration and cognitive decline: exploring interactions with biomarkers of Alzheimer disease. *JAMA Neurol.* **72**, 520–529 (2015).
38. Woods, N. F., Mitchell, E. S., Coslov, N. & Richardson, M. K. Transitioning to the menopausal transition: a scoping review of research on the late reproductive stage in reproductive aging. *Menopause* **28**, 447–466 (2021).
39. Yan, F. et al. The role of oxidative stress in ovarian aging: a review. *J. Ovarian Res* **15**, 100 (2022).
40. Amorim, J. A. et al. Mitochondrial and metabolic dysfunction in ageing and age-related diseases. *Nat. Rev. Endocrinol.* **18**, 243–258 (2022).
41. Harguindegay, A. et al. Synthesis and assembly of click-nucleic-acid-containing PEG-PLGA nanoparticles for DNA delivery. *Adv. Mater.* **29**, <https://doi.org/10.1002/adma.201700743> (2017).
42. Jeon, S. Y., Park, J. S., Yang, H. N., Woo, D. G. & Park, K. H. Co-delivery of SOX9 genes and anti-Cbfa-1 siRNA coated onto PLGA nanoparticles for chondrogenesis of human MSCs. *Biomaterials* **33**, 4413–4423 (2012).
43. Shive, M. S. & Anderson, J. M. Biodegradation and biocompatibility of PLA and PLGA microspheres. *Adv. Drug Deliv. Rev.* **28**, 5–24 (1997).
44. Harrell, C. R. et al. Molecular mechanisms responsible for therapeutic potential of mesenchymal stem cell-derived secretome. *Cells* **8**, <https://doi.org/10.3390/cells8050467> (2019).
45. Lagreca, E. et al. Recent advances in the formulation of PLGA microparticles for controlled drug delivery. *Prog. Biomater.* **9**, 153–174 (2020).
46. Hirota, K. et al. Optimum conditions for efficient phagocytosis of rifampicin-loaded PLGA microspheres by alveolar macrophages. *J. Control. Release* **119**, 69–76 (2007).
47. Palikaras, K., Lionaki, E. & Tavernarakis, N. Mechanisms of mitophagy in cellular homeostasis, physiology and pathology. *Nat. Cell Biol.* **20**, 1013–1022 (2018).
48. Castrillon, D. H., Miao, L., Kollipara, R., Horner, J. W. & DePinho, R. A. Suppression of ovarian follicle activation in mice by the transcription factor Foxo3a. *Science* **301**, 215–218 (2003).
49. Matsuda, F., Inoue, N., Manabe, N. & Ohkura, S. Follicular growth and atresia in mammalian ovaries: regulation by survival and death of granulosa cells. *J. Reprod. Dev.* **58**, 44–50 (2012).
50. Meng, L. et al. Transcriptome analysis of porcine granulosa cells in healthy and atretic follicles: role of steroidogenesis and oxidative stress. *Antioxidants* **10**, <https://doi.org/10.3390/antiox10010022> (2020).
51. Miller, W. L. Steroid hormone synthesis in mitochondria. *Mol. Cell. Endocrinol.* **379**, 62–73 (2013).
52. Miller, W. L. Disorders in the initial steps of steroid hormone synthesis. *J. Steroid Biochem. Mol. Biol.* **165**, 18–37 (2017).
53. Karnezis, A. N. et al. Re-assigning the histologic identities of COV434 and TOV-112D ovarian cancer cell lines. *Gynecol. Oncol.* **160**, 568–578 (2021).
54. Klionsky, D. J., Cuervo, A. M. & Seglen, P. O. Methods for monitoring autophagy from yeast to human. *Autophagy* **3**, 181–206 (2007).
55. Ostuni, A., Faruolo, M. P., Sileo, C., Petillo, A. & Boni, R. Effect of follicle size and atresia grade on mitochondrial membrane potential and steroidogenic acute regulatory protein expression in bovine granulosa cells. *Zygote* **26**, 476–484 (2018).
56. Lu, L. et al. Glyphosate-induced mitochondrial reactive oxygen species overproduction activates parkin-dependent mitophagy to inhibit testosterone synthesis in mouse Leydig cells. *Environ. Pollut.* **314**, 120314 (2022).
57. Ashrafi, G. & Schwarz, T. L. The pathways of mitophagy for quality control and clearance of mitochondria. *Cell Death Differ.* **20**, 31–42 (2013).
58. Bravo-San Pedro, J. M., Kroemer, G. & Galluzzi, L. Autophagy and mitophagy in cardiovascular disease. *Circ. Res.* **120**, 1812–1824 (2017).
59. Zou, L. et al. Copper nanoparticles induce oxidative stress via the heme oxygenase 1 signaling pathway in vitro studies. *Int. J. Nanomed.* **16**, 1565–1573 (2021).
60. Wang, Y. et al. HO-1 reduces heat stress-induced apoptosis in bovine granulosa cells by suppressing oxidative stress. *Aging* **11**, 5535–5547 (2019).
61. Tatone, C. et al. Age-dependent changes in the expression of superoxide dismutases and catalase are associated with ultrastructural modifications in human granulosa cells. *Mol. Hum. Reprod.* **12**, 655–660 (2006).
62. Baiioni, L., Basini, G., Bussolati, S. & Grasselli, F. Stanniocalcin 1 affects redox status of swine granulosa cells. *Regul. Pept.* **168**, 45–49 (2011).
63. Liu, G. et al. Stanniocalcin 1 and ovarian tumorigenesis. *J. Natl. Cancer Inst.* **102**, 812–827 (2010).

64. Paciga, M., DiMattia, G. E. & Wagner, G. F. Regulation of luteal cell big stanniocalcin production and secretion. *Endocrinology* **145**, 4204–4212 (2004).
65. Luo, C. W., Kawamura, K., Klein, C. & Hsueh, A. J. Paracrine regulation of ovarian granulosa cell differentiation by stanniocalcin (STC) 1: mediation through specific STC1 receptors. *Mol. Endocrinol.* **18**, 2085–2096 (2004).
66. Juengel, J. L., Heath, D. A., Quirke, L. D. & McNatty, K. P. Oestrogen receptor alpha and beta, androgen receptor and progesterone receptor mRNA and protein localisation within the developing ovary and in small growing follicles of sheep. *Reproduction* **131**, 81–92 (2006).
67. Billig, H., Furuta, I. & Hsueh, A. J. Estrogens inhibit and androgens enhance ovarian granulosa cell apoptosis. *Endocrinology* **133**, 2204–2212 (1993).
68. Taipale, J. et al. Effects of oncogenic mutations in smoothened and patched can be reversed by cyclopamine. *Nature* **406**, 1005–1009 (2000).
69. Victorelli, S. et al. Apoptotic stress causes mtDNA release during senescence and drives the SASP. *Nature* **622**, 627–636 (2023).
70. Macklon, N. S. & Fauser, B. C. Aspects of ovarian follicle development throughout life. *Horm. Res.* **52**, 161–170 (1999).
71. Vanderhyden, B. C., Telfer, E. E. & Eppig, J. J. Mouse oocytes promote proliferation of granulosa cells from preantral and antral follicles in vitro. *Biol. Reprod.* **46**, 1196–1204 (1992).
72. Robertson, D. M., Lee, C. H. & Baerwald, A. Interactions between serum FSH, inhibin B and antral follicle count in the decline of serum AMH during the menstrual cycle in late reproductive age. *Endocrinol. Diab. Metab.* **4**, e00172 (2021).
73. Wen, J. et al. Can inhibin B reflect ovarian reserve of healthy reproductive age women effectively?. *Front. Endocrinol.* **12**, 626534 (2021).
74. Burger, H. G., Dudley, E., Mamers, P., Groome, N. & Robertson, D. M. Early follicular phase serum FSH as a function of age: the roles of inhibin B, inhibin A and estradiol. *Climacteric* **3**, 17–24 (2000).
75. Klein, N. A. et al. Age-related analysis of inhibin A, inhibin B, and activin a relative to the intercycle monotropic follicle-stimulating hormone rise in normal ovulatory women. *J. Clin. Endocrinol. Metab.* **89**, 2977–2981 (2004).

Acknowledgements

We extend our gratitude to all co-authors for their invaluable contributions to this manuscript. This work was supported by Sanming Project of Medicine in Shenzhen (No. SZSM20211016), Scientific Research Foundation of Peking University Shenzhen Hospital (No. KYQD2021075), Shenzhen High-level Hospital Construction Fund (YBH2019-260), the National Natural Science Foundation of China (U1812403 to L.G.) and the National Natural Science Foundation of China (82293683 to X.H.).

Author contributions

Conceptualization: L.G., B.T., and X.H., Methodology: L.G., J.S., Q.Z., K.L., Q.S., L.B., Y.D. B.T., and X.H., Investigation: L.G., J.S., Q.Z., K.L., Q.S., L.B., Y.D., B.T., and X.H., Visualization: L.G., J.S., and Q.Z., Supervision: L.G., B.T., X.H., C.L. Writing original draft: L.G., Writing editing and review: L.G., J.S., Q.Z., H.P., B.T., and X.H.

Competing interests

The authors declare no competing interests.

Additional information

Supplementary information The online version contains supplementary material available at <https://doi.org/10.1038/s42003-025-08576-w>.

Correspondence and requests for materials should be addressed to Liming Gui, Bin Tang, Xiaojiang Hao or Changzhong Li.

Peer review information *Communications Biology* thanks Joanna Poulton, Yanzhou Yang, and Ozgur Oktem for their contribution to the peer review of this work. Primary Handling Editor: Dario Ummarino. A peer review file is available.

Reprints and permissions information is available at <http://www.nature.com/reprints>

Publisher's note Springer Nature remains neutral with regard to jurisdictional claims in published maps and institutional affiliations.

Open Access This article is licensed under a Creative Commons Attribution-NonCommercial-NoDerivatives 4.0 International License, which permits any non-commercial use, sharing, distribution and reproduction in any medium or format, as long as you give appropriate credit to the original author(s) and the source, provide a link to the Creative Commons licence, and indicate if you modified the licensed material. You do not have permission under this licence to share adapted material derived from this article or parts of it. The images or other third party material in this article are included in the article's Creative Commons licence, unless indicated otherwise in a credit line to the material. If material is not included in the article's Creative Commons licence and your intended use is not permitted by statutory regulation or exceeds the permitted use, you will need to obtain permission directly from the copyright holder. To view a copy of this licence, visit <http://creativecommons.org/licenses/by-nc-nd/4.0/>.

© The Author(s) 2025